Master of Science by Dissertation:
Subspace Tracking, Discrimination of Unexploded Ordinances (UXO) in Airborne Magnetic Field Gradients

Mark Jeoffreys (9807515F)
Supervisor: Dr Neil Pendock

2005

Abstract

Statistical and algebraic techniques of subspace tracking were tested for filtering the earth’s response from airborne magnetic field gradients in order to discriminate the relatively small response (dipole) of objects on the earth’s surface, such as UXO. Filtering the data was not very effective with these methods but a subspace was found in the data for the magnitude of the magnetic moment of the dipole. This subspace is easily obtained using the singular value decomposition and can be used for an approximate location, without depth estimation, as well as the relative size of the dipole.

Declaration

I declare that this dissertation is my own, unaided work. It is being submitted for the Degree of Master of Science in the University of the Witwatersrand, Johannesburg. It has not been submitted before for any degree or examination in any other University.

____
(Mark Jeoffreys)

8th day of March 2006

Contents

List of Figures

Chapter 1

Introduction

1.1 Landmines

Since 1975, landmines have exploded under more than 1 million people and are claiming over 500 victims a week [11; 28]. There are an estimated 120 million uncleared landmines in the fields and alongside the roads and footpaths of 87 of the countries in the developing world. Aside from the enormous pain and suffering, landmines also bring economic and social costs, the expense of medical treatment, the cost to families of caring for injured relatives, hindering the flow of goods and people, and put huge areas of agricultural land out of production.

> *a land-mine is a perfect soldier: Ever courageous, never sleeps, never misses.*
> Khmer Rouge general

Clearing landmines is a laborious, dangerous and enormously expensive task. Weapons that can cost less than US$3 each to manufacture can cost up to US$1,000 each to clear. Clearing requires vegetation cutters to clear the terrain, trained workers have to crawl their way along, probing the soil ahead inch by inch, and sometimes dogs are used to locate the mines by scent. One person can clear only 20 to 50 square metres per day. Sometimes heavy equipment, such as flails and rollers are used to limited success but unfortunately de-mining technology has not caught up with the advances in mine manufacturing technology. Many plastic landmines exist and the majority of landmines manufactured today are not particularly magnetic but a large amount of the landmines left behind in countries like Mozambique and Cambodia are old and, along with mortar shells, do have a significant magnetic field which can be detected. This is just one tool and knowledge of what to expect an area is needed to decide what tools to use. There are tools which use the likes of thermal sensors and even vegetation which changes colour though a chemical reaction with any leaking explosive.

1.2 Magnetic Field Sensors

Modern sensors are capable of detecting, from an airborne platform, the small variations in the magnetic field gradients caused by magnetic dipoles located close to the earth's surface. These sensors have a wide range of applications: airborne detection of unexploded ordinances (UXO) such as landmines and mortar shells, surveying for minerals or archaeological sites, as well as external monitoring of a foetal heart rate. Although each application has different requirements, which will be discussed later, they all involve the discrimination of the relevant source from the earth's magnetic field - which is three orders of magnitude greater than that of any objects located near the surface of the earth - as well as any additional noise. The research proposed to evaluate different subspace tracking methods for the discrimination of the source (dipoles) and its properties, the magnetic moment and the location. In UXO detection the location is very important and for the classification of the UXO the magnetic moment is important. In surveying, the exact location is not as crucial as with UXO detection, but consistency in the relative magnitudes for the moments over the survey area is important and this requires data compensation for variation in the altitudes of flight paths over the area. In a foetal heart rate monitor, the location is of little importance, only the variation in the magnetic moment is of interest.

1.3 Subspace Tracking

Signals can be a combination of multiple sources and can also suffer from interference (noise) [14]. Subspace tracking is a blind method for the decomposition of the sources as well as the noise into separate channels. Subspace tracking methods have been used in many signal processing applications to decompose the data into the sources and the mixing matrix [19; 26; 30]. The linear mixing model is presented in section 2.3. This model assumes that the data is a superposition of sources with added noise and that the sources remain stationary across the length of the data. The stationary assumption requires that windows of data are used in processing in order to reduce the effects of averaging of the flight path.

1.4 Research Outline

This research focused on the use of subspace tracking methods as a process for filtering out the effects of the earth's magnetic field in the magnetic field gradient data and thus locating the surface dipole (UXO). This is presented over the remaining four chapters of this report. Chapter 2 (Background and Related Work) describes the equations of magnetic fields and a brief explanation of Frahm's [9] inversion for the magnetic field gradients. Related work on UXO discrimination and classification in total magnetic field data is discussed in section 2.2 and in section 2.3 the proposed methods of subspace tracking, which were tested, are explained. The chapter, following the background, discusses the research methodology. How the simulated data was created, the use of different window sizes for filtering, the inversion methods and finally the estimation of the dipole properties. The results, from the tests, are presented and discussed in chapter 4, and the last chapter is a summary of the work and findings.

Chapter 2

Background and Related Work

2.1 Introduction

In the introduction chapter, there is mention of the devastation caused by landmines as well as the lack of technology to aid in the clearing of minefields. Research into the use of magnetic surveying has proven that it is a very useful tool for the locating and identifying of UXO. This research, which is discussed in the first part of this chapter, uses total magnetic field surveys measured close to the surface of the earth. Due to the dangers of obtaining such data in live landmine fields, an airborne survey is a far safer and more efficient option. However, total magnetic field data from an airborne platform cannot discriminate such small anomalies. Magnetic field gradients can be used to improve the resolution of magnetic field maps [10] and are sensitive enough to pick up the changes in the magnetic field gradients, from an airborne platform, caused by small anomalies. The research tested a number of subspace tracking techniques for compensating the magnetic field gradients in order to discriminate surface objects (UXO). The methods are explained in section 2.3 as well as a brief description of subspace estimation and the assumed linear mixing model. The explanation for assumed linear models, given in section 2.5, are based on the magnetic field gradient equations which are defined in section 2.4.2 along with an analytical inversion for the gradients.

2.2 UXO Classification

Magnetic and electromagnetic are well established methods for the detection of UXO [4], as they are very effective at locating metallic objects buried near the surface of the earth. Billings [1; 2; 3] deals with the challenging task of discriminating between UXO and other metallic objects, by using a library of feasible curves for the expected UXO in the survey area. An estimate for an object's remanent magnetisation (the permanent magnetisation that remains after the external field is removed) is given by the minimum distance between the recovered dipole moment and the feasibility curves. The UXO likelihood of the anomalies can then be ranked based on their remanence. In testing [3] the discrimination using remanence achieved 100% UXO detection with less than 20% of other objects incorrectly classed as UXO and a false-alarm rate (FAR) of less than 2. FAR is the number of non-UXO removed per UXO.

2.3 Subspace Tracking Methods

2.3.1 Subspace Estimation

The measured data is a mixture of data from different sources as well as noise. This can be written in the equation

$$Y = D(\theta)S + \mathcal{N}, \tag{2.1}$$

where Y is the measured values for the n sensors, S is the values for the m sources ($m \leq n$), $\mathcal{N}$ is the noise matrix and $D(\theta)$ is a $m \times n$ mixing matrix with the parameters θ. In analysis for direction of arrival these parameters give the directions to the sources. The noise matrix $\mathcal{N}$ can be dropped by assuming that the noise is an additional source. The sources (subspaces) can now be determined by decomposing the matrix Y, into the matrices D and S. This matrix decomposition can be done with algebraic or statistical methods and the techniques applied in this research are defined in the remainder of this section.

2.3.2 Singular Value Decomposition

The singular value decomposition (SVD) [25] is a common tool in signal processing. Its use in subspace tracking is discussed in [18; 29].

Let A denote an $m \times n$ matrix of real-valued data and rank r, where without loss of generality $m \geq n$, and therefore $r \leq n$. The equation for singular value decomposition of A is the following:

$$A = USV^T, \tag{2.2}$$

where U is an $m \times n$ orthonormal matrix, S is an $n \times n$ diagonal matrix, and V^T is an $n \times n$ orthonormal matrix. The elements of S are the singular values of A and $S = \text{diag}(s_1, ..., s_n)$, $s_i > 0$ for $1 \leq i \leq r$, and $s_i = 0$ for $(r+1) \leq i \leq n$. By convention, the ordering of the singular vectors is determined by high-to-low sorting of singular values, i.e. $s_1 \geq s_2 \geq \ldots \geq s_n$. The columns of U are the principal components, or subspaces, of the matrix A.

2.3.3 UTV Decompositions

The SVD has the drawback of high computational costs when updating. The UTV decompositions [6; 17; 24], are rank revealing two-sided orthogonal decompositions which are easier to update than the SVD. The middle matrix of the UTV is triangular. The case where the middle matrix is lower triangular is called the ULV and has the form:

$$A = U_L L V_L^T \tag{2.3}$$

where U_L is an $m \times n$ orthonormal matrix, L is an $n \times n$ lower triangular matrix, and V_L^T is an $n \times n$ orthonormal matrix. Note the ULV decomposition of A is not unique and the SVD is a special case of the ULV.

2.3.4 Maximum Likelihood Estimation

The SVD and ULV both result in orthogonal subspaces. This causes difficulties when the signals are highly correlated, as is the case with the components of the magnetic moments. Maximum likelihood (ML) estimation does not require orthogonal bases so it is possible to find the different directional component of the magnetic moments as separate signals, which should also simplify the direction of arrival estimation. A draw back of such statistical methods is the dependance on the signal to noise ratio (SNR), which if small makes success improbable. Rewrite (2.1) as the time dependent system

$$y(t) = D(\theta)s(t) + n(t). \tag{2.4}$$

If the parameterization $D(\theta)$ is completely known, unambiguous and we assume that the noise is uncorrelated with the signals and spatially white, i.e. $E[n(t)n(t)^T] = \sigma^2 I$, then the covariance of the data is defined as

$$R = \lim_{N\to\infty} \frac{1}{N} \sum_{i=1}^{N} y(t_i)y(t_i)^T = D(\theta)\Lambda D(\theta)^T + \sigma^2 I, \tag{2.5}$$

where

$$\Lambda = \lim_{N\to\infty} \frac{1}{N} \sum_{i=1}^{N} s(t_i)s(t_i)^T. \tag{2.6}$$

The sample estimate of R is

$$\hat{R} = \frac{1}{N} \sum_{k=1}^{N} y(t_k)y(t_k)^T, \tag{2.7}$$

where N is the window size. Then the ML solution can be determined by maximizing the log-likelihood function over θ which is equivalent to [12]

$$\hat{\theta} = \arg\min_{\theta} \log \left(\det \left[P_D \hat{R} P_D - \frac{\mathrm{Tr}(P_D^{\perp}\hat{R})}{m-n} P_D^{\perp} \right] \right), \tag{2.8}$$

where the projection matrix $P_D = I - P_D^{\perp}$ is defined as

$$P_D = D(\theta)[D(\theta)^T D(\theta)]^{-1} D(\theta)^T. \tag{2.9}$$

Alternatively [26]

$$\hat{\theta} = \arg\min_{\theta} \mathrm{Tr} \left[P_D^{\perp}(\hat{R} + \hat{\sigma}^4 \hat{R}^{-1} - 2\hat{\sigma}^2 I) \right], \tag{2.10}$$

where $\hat{\sigma}^2$ is an estimate for the noise.

2.3.5 Bayesian Geometric Estimation

Srivastava [22; 23] describes a geometric approach to subspace estimation, of the time dependent system (2.4), with each subspace represented by its unique projection on a complex Grassmann manifold [16]. Subspace tracking then corresponds to the inferences on the unitary group ($\mathbf{U}(n)$), where the variation between the subspaces is modeled by rotating the projection matrices via the action of unitary matrices. If P_1 and P_2 are the projection matrices representing two distinct subspaces, then there exists a rotation U such that $P_2 = U^T P_1 U$ and every projection matrix can be represented as a rotation of some pre-selected projection. Thus the whole space of $n \times n$, rank-m projection matrices, $\mathcal{P}$, can be generated by applying rotations to a chosen projection, Q. For simplicity, let Q be the $n \times n$ matrix with all zeros except for the first m diagonal entries, which are all ones. Let γ be the rotation-invariant Haar measure [5] with respect to which the posterior density on $\mathbf{U}(n)$ is defined. Then the posterior density on $\mathbf{U}(n)$ is defined as

$$\pi(U|y) = \frac{\exp\{\frac{N}{\sigma^2}(\mathrm{Tr}(U^T Q U \hat{R}))\}\pi_0(U)}{\int_{\mathbf{U}(n)} \exp\{\frac{N}{\sigma^2}(\mathrm{Tr}(U^T Q U \hat{R}))\}\pi_0(U)\gamma(dU)}, \tag{2.11}$$

where π_0 is a prior density on $\mathbf{U}(n)$ and for example can be

$$\pi_0 \propto \exp(-\frac{1}{\sigma_p^2}\|U^T Q U - P_0\|^2), \tag{2.12}$$

where P_0 is predicted from prior knowledge.

2.4 Magnetic Fields

2.4.1 Magnetic Field Equations

The magnetic field $\mathbf{H}$ for a magnetic dipole with magnetic moment $\mathbf{m}$ is given by

$$\mathbf{H} = \frac{3(\mathbf{m}\cdot\mathbf{r})\mathbf{r}}{r^5} - \frac{\mathbf{m}}{r^3}, \tag{2.13}$$

where $\mathbf{r}$ is the position vector of the field point relative to the dipole and r is the magnitude of $\mathbf{r}$. Equivalently in index form, adopting Einstein's summation convention

$$H_j = \frac{3m_i r_i r_j}{r^5} - \frac{m_j}{r^3}. \tag{2.14}$$

Differentiating with respect to the coordinates of the field point,

$$\partial_j H_k = M_i N_{ijk}, \tag{2.15}$$

where $\partial_1 = \partial/\partial_x$, $\partial_2 = \partial/\partial_y$, $\partial_3 = \partial/\partial_z$, $M_i = 3m_i/r^4$ and N_{ijk} is a completely symmetric third rank tensor given by

$$N_{ijk} = 5n_i n_j n_k - (\delta_{ki} n_j + \delta_{kj} n_i + \delta_{ji} n_k), \tag{2.16}$$

where $n_i = r_i/r$. The magnetic field gradients must obey Maxwell's equations in a vacuum.

$$\begin{aligned} \partial_j H_j &= 0, & (2.17) \\ \partial_j H_k &= \partial_k H_j. & (2.18) \end{aligned}$$

Thus there are only 5 linearly independent field gradients.

2.4.2 Inversion

The magnetic field gradient equations in the previous section have been expressed in index notation and are invariant to rotations of the axes. The Frahm inversion [9] uses this property by finding the solution in a reference frame of the principal axes in which $\partial_j H_k$ is diagonal. These diagonal elements, denoted ∂H_l, are the eigenvalues of the matrix A whose elements are given by

$$A_{ij} = \partial_i H_j, \tag{2.19}$$

such that

$$\partial H_1 \partial H_2 \geq 0, \tag{2.20}$$

and

$$|\partial H_1| \geq |\partial H_2|. \tag{2.21}$$

The rotation from the measurement frame to the reference frame, R, is defined by the corresponding eigenvectors and the relationships between quantities in the two frame are given by

$$n_l = \frac{\bar{n_i}}{R_{il}}, \tag{2.22}$$

and

$$M_l = \frac{\bar{M_i}}{R_{il}}, \tag{2.23}$$

where bars denote quantities in the reference frame. Then the Frahm inversion is given by

$$\begin{aligned}
\bar{n_1} &= \eta_1 \sqrt{(a-b)/a}, &(2.24)\\
\bar{n_2} &= 0, &(2.25)\\
\bar{n_3} &= \eta_3 \sqrt{b/a}, &(2.26)
\end{aligned}$$

and

$$\begin{aligned}
\bar{M_1} &= \frac{1}{3}\eta_1 (5b-a)\sqrt{(a-b)/a}, &(2.27)\\
\bar{M_2} &= 0, &(2.28)\\
\bar{M_3} &= \frac{1}{3}\eta_3 (5b-4a)\sqrt{b/a}, &(2.29)
\end{aligned}$$

where $a = 2\partial H_1 + \partial H_2$, $b = \partial H_1 + 2\partial H_2$, $\eta_1 = \pm 1$ and $\eta_3 = \pm 1$. Thus, there are four symmetric solutions corresponding to the permutations of η_1 and η_3. Simple logic can be used to eliminate the ghost solutions that appear in midair but there is still ambiguity in the solution. These ambiguities and the requirement to first compensate the data for the earth's magnetic field make such an inversion undesirable.

2.4.3 Euler Deconvolution

Euler deconvolution can be used to assist in the interpretation of magnetic survey data [8]. Given a homogeneous function $f(\mathbf{v})$ with degree of homogeneity n. The degree of homogeneity is dependent on the type of source and characterizes how quickly the strength of field decreases relative to the distance from the source. Now if

$$f(t\mathbf{v}) = t^n f(\mathbf{v}), \tag{2.30}$$

where t is an element of the reals. The Euler's equation, if f is differentiable at $\mathbf{v}$, is

$$\mathbf{v}\nabla_{\mathbf{v}} f(\mathbf{v}) = n f(\mathbf{v}), \tag{2.31}$$

and solving in the appropriate cases, Euler deconvolution. A field f, which has the form

$$F = \frac{A}{r^{-N}}, \tag{2.32}$$

is homogeneous of degree $-N$ ($N = -n$). For convenience the structural index (SI) is defined as N and in the case of the magnetic field produced by a dipole, where the field decreases relative to inverse distance cubed, the SI is 3 (the degree of homogeneity $n = -3$). Euler's equation, for the magnetic field B observed at point (x, y, z), can be expressed in the form [27]

$$(x - x_0)\frac{\partial B_i}{\partial x} + (y - y_0)\frac{\partial B_i}{\partial y} + (z - z_0)\frac{\partial B_i}{\partial z} = -NB_i, \tag{2.33}$$

where (x_0, y_0, z_0) is the location of the source and N is the SI. The extended Euler deconvolution [20] uses the Hilbert transform to derive further formula that can then be used to solve for the SI as well as the location of the magnetic anomaly. It is applied to total magnetic field data for the detection of UXO by [7] by marking anomalies with SI close to 3 as possible UXO.

2.5 Linear Models of Magnetic Field Gradients

The research applies subspace tracking, with a linear mixing model (equation (2.1)), in order to extract both the location of the magnetic source as well as the properties of the magnetic moment from the magnetic field gradients. Equation (2.15) defines the magnetic field gradients and is linear in M_i and thus, assuming no noise, the model of the gradients could be defined as

$$G = NM \tag{2.34}$$

where G is the vector of gradients $\partial_j H_k$, N is the mixing matrix corresponding to the third rank tenor N_{ijk}, given in equation (2.16), and M is a matrix of three subspaces , M_i, which are directly proportional to the components of the magnetic moment divided by the cube of the distance from the dipole. This linear model decomposes the gradients into a mixing matrix, which has parameters for the direction to the source, and the subspaces, which are directly proportional to the total magnetic field of the source and inversely proportional to the fourth power of the distance from the source. An alternative linear model for the magnetic field gradients can be given with only one subspace. Define

$$P_i = \frac{3m_i}{m} \tag{2.35}$$

where m is the magnitude of the magnetic moment **m**.

Then equation (2.15) can be written as

$$\partial_j H_k = \frac{m}{r^4} N_{ijk} P_i \tag{2.36}$$

which is linear in m/r^4. The gives a model with a single column mixing matrix, which has parameters for the direction to the source as well as the orientation of the magnetic moment, corresponding to the sum $N_{ijk}P_i$ and a single subspace which is directly proportional to the magnitude of the magnetic moment and inversely proportional to the fourth power of the distance from the source. The magnitude of the magnetic moment of objects close to the surface of the earth can be assumed constant and thus the subspace will peak when closest to the source.

Chapter 3

Methodology

3.1 Introduction

The problem of landmines and their removal has been mentioned in the introduction chapter, and in the previous chapter research relating to the locating and classifying of UXO using total magnetic fields is discussed, as well as defining the subspace tracking techniques which this research evaluated for the purpose of locating UXO in airborne magnetic field gradients. This chapter explains the main aspects of the experimentation that was done for this evaluation. When evaluating and comparing different techniques, it is necessary to have some criteria upon which the evaluation can be based. The criteria used are presented in section 3.2. These criteria required knowing the exact solution which was most easily obtained by using simulated data as described in section 3.4. The earth's response was filtered from the data based on a linear mixing model. Section 3.5 justifies the use this model in the compensation and section 3.6 explains how the inversion of the compensated data was done in order to get the set of direction vectors to the dipole as well as the magnetic moment vectors of the dipole. This set was then used to create an estimate for the location and moment of the dipole using the algorithm outlined in the final section of the chapter.

3.2 Evaluation of Subspace Tracking Methods

The research did not have a set hypothesis but was rather an investigation into the use of subspace tracking for the filtering of the magnetic field gradient data which proposed to evaluate and compare different methods of subspace tracking for the discrimination of magnetic dipoles, possible UXO, in airborne magnetic field gradients. The following points were considered in evaluating the methods:

- Accuracy of the location estimation
- Accuracy of the magnetic moment estimation
- Effect of data window size
- Robustness to noise

3.3 Measured Data

The measured data was recorded using a SQUID gradiometer, which was toed below a helicopter. The SQUID gradiometer records 6 magnetic gradients. In order to improve the precision of the gradiometer the gradients sensors are not arranged orthogonally and a rotation is used to get the gradients, $\partial_j H_k$, in the Euclidian basis. Along with the 6 gradient measures, the toe also included total field sensors for the three magnetic field components and a gps system to record the sensors' location.

3.4 Simulated Data

In order to evaluate the accuracy of the methods, a prior knowledge of the correct solution is preferred. In order to get a variety of data conditions with this knowledge, it was necessary to construct simulated data. The data was constructed by using measured data that had no sign of a dipole in it for the earth's magnetic field and adding the effect of a dipole to the data using the forward equations for the magnetic field gradients and the flight path of the measured earth data. The dipole was placed randomly on the ground within a 0.02 kilometre strip along the flight path. In [13] it was found that a varying flight path adversely effected results and thus both smooth and rough flight paths, which height between 8 and 15 metres, were used in test data.

3.5 Compensation

From equation (2.15), section 2.4.1, the magnetic field gradients are a linear combination of the magnetic moment's components. Then using a linear mixing model (equation (2.1), section 2.3.1), for the magnetic field gradient data, the magnetic moment's components are the sources, S, and the parameters, θ, of the mixing matrix, D, are the directions of arrival. Also the magnetic moment's components are inversely proportional to the fourth power of the distance from the moment, in equation (2.15), and so as the distance decreases the strength of the source will increase and visa-versa. If the sensor is close to a UXO the magnetic gradient of the dipole should be large compared with the gradient of the earth and when not close to the target it will not be detected. When decomposing the magnetic gradient data using the SVD, the three most significant subspaces had a high correlation with the three components of the recorded total magnetic field, which can be expected since the measured magnetic field gradients will generally be from the changes in the earth's magnetic field which is the strongest source and from equation (2.34) in section 2.5 the magnetic field gradients decompose into the total magnetic field divided by the fourth power of the distance but the distance to the earth is relatively constant (the aircraft will also be a strong component, with small variation due to turbulence but a rather constant magnitude, and is possibly included in the first three subspaces). The fourth subspace shows isolated spikes which are the results of the increase and decrease the response strength of the sources as the distance changes while flying over it (see the alternative linear model in section 2.5. The remaining two subspaces have significantly smaller singular values and could be noise. Having only one subspace for the desired dipoles can be expected since the subspaces are orthonormal, by definition of the SVD (section 2.3.2), and the measure of three components of the dipoles are not independent. Thus the orientation of the magnetic moment as well as the direction to the dipole are properties of the mixing matrix D and logically if the subspace is a scaled magnitude of the dipoles then the structure of D corresponding to the subspace is the appropriately scaled magnetic field gradient equations. However, since D is constant, any movement in the directions of and to the dipole over the measuring period of Y will be averaged in some way. In order to track the movement of the dipole relative to the platform, small windows of the data are required to reduce the averaging but the smaller the window the less data there is to help distinguish the different subspaces. An aspect of the research was to determine the best window size to balance these problems. The windows were shifted along the data one point at a time and only the results from the middle of each window were used in the inversion.

3.6 Inversion

The SVD and ULV methods decompose the data into the subspace which can then be filtered by synthesizing only the relevant subspaces. This filtered data must then be inverted in order to locate the dipole and was done using the Frahm algorithm [9] (section 2.4.2), with the ghosts eliminated by choosing the deepest solution at each point. Alternatively optimization techniques, as in [21], can be used to find a solution from the filtered data. In the cases of the maximum likelihood and geometric subspace tracking techniques the parameters over which they are optimised include the unit direction vectors to the dipole and the vectors for the magnetic moment of the dipole so the inversion is performed as part of the filtering process. This required the definition of the direction matrix in terms of these parameters for calculating the projection matrix, in equation (2.9). The direction matrix was defined with three subspaces for the earth's response and three subspaces to represents the dipole, one for each of the components of the magnetic moment.

$$D(\theta) = \begin{bmatrix} N^e_{111} & N^e_{211} & N^e_{311} & N^d_{111} & N^d_{211} & N^d_{311} \\ N^e_{112} & N^e_{212} & N^e_{312} & N^d_{112} & N^d_{212} & N^d_{312} \\ N^e_{113} & N^e_{213} & N^e_{313} & N^d_{113} & N^d_{213} & N^d_{313} \\ N^e_{122} & N^e_{222} & N^e_{322} & N^d_{122} & N^d_{222} & N^d_{322} \\ N^e_{123} & N^e_{223} & N^e_{323} & N^d_{123} & N^d_{223} & N^d_{323} \end{bmatrix} \tag{3.1}$$

where $N^e_{ijk} = 5n^e_i n^e_j n^e_k - (\delta_{jk}n^e_i + \delta_{ki}n^e_j + \delta_{ij}n^e_k)$, $N^d_{ijk} = 5n^d_i n^d_j n^d_k - (\delta_{jk}n^d_i + \delta_{ki}n^d_j + \delta_{ij}n^d_k)$, and $\mathbf{n}^e$ and $\mathbf{n}^d$ are the unit direction vector to the magnetic moments of the earth and dipole respectively. Due to the lack of convergence with this $D(\theta)$ a second representation with only one subspace for the dipole was tested. The single subspace is the magnitude of the magnetic moment and the orientation of the magnetic moment is contained in the mixing matrix, $D(\theta)$, with the parameterization:

$$D(\theta) = \begin{bmatrix} N^e_{111} & N^e_{211} & N^e_{311} & m_1N^d_{111} + m_2N^d_{211} + m_3N^d_{311} \\ N^e_{112} & N^e_{212} & N^e_{312} & m_1N^d_{112} + m_2N^d_{212} + m_3N^d_{312} \\ N^e_{113} & N^e_{213} & N^e_{313} & m_1N^d_{113} + m_2N^d_{213} + m_3N^d_{313} \\ N^e_{122} & N^e_{222} & N^e_{322} & m_1N^d_{122} + m_2N^d_{222} + m_3N^d_{322} \\ N^e_{123} & N^e_{223} & N^e_{323} & m_1N^d_{123} + m_2N^d_{223} + m_3N^d_{323} \end{bmatrix} \tag{3.2}$$

With N^e_{ijk}, N^d_{ijk}, $\mathbf{n}^e$ and $\mathbf{n}^d$ as above, and $\mathbf{m}$ is the unit direction vector of the dipole's magnetic moment. Both techniques also require an estimate for the variance of the noise and so experimentation was done with a different estimates for the variance to determine best results. Since the geometric subspace tracking technique is a Bayesian method it requires a prior distribution which was defined as in equation (2.12) with the matrix P_0 being the measured total magnetic field for the earth's response subspaces and zero for the dipole's subspace(s). The posterior was then solved using the sequential Monte Carlo method [15] with the extrinsic mean as in [23].

Experimentation with both methods on a range of variances had either slow or non-existent convergence. This has been put down to the assumption that the noise is spatially white being incorrect and is discussed further in the results chapter.

3.7 Estimation

The results of the inversions are a set of unit direction vectors to the dipole and the vectors for the magnetic moment of the dipole with a scaled magnitude, from each sample point. Before calculating an estimate for the dipole's location and magnetic moment it is then necessary to divide the vectors from this set into two classes, those associated with the dipole and those which are just background. This was done by using a threshold on the scaled magnitude of the dipole. Now the set of vectors associated with the dipole is used to estimate its location. A possible method for doing this is by finding the intersection of the unit direction vectors extended from their sampling locations. Since these will not all intersect at one point a least squares solution can be taken. The mean of the magnetic moment vectors, scaled for the estimated distance, can be used as an estimate for the magnetic moment. Alternatively the estimate for the moment can be calculated from the data as this is a linear problem using the estimated location. This method for calculating the location was not used, since UXO are generally on the ground or just below the surface, the problem of depth estimation can be avoided by fixing the depth of the UXO at ground level. Having fixed the depth of the estimate each of the unit direction vectors are extended from their sampling locations to intersect with the plane, creating a set of points on the plane, and these points of intersection are used to estimate the location of the dipole by taking their mean position. Misclassified sample points produce outlying points of intersection which can skew the estimate and so the following algorithm was used to reduce the shifting from outliers:

Step 1 Calculate the mean and variance of the set of intersection points

Step 2 If the variance is below a given tolerance then go to step 5

Step 3 Find the intersection point furthers from the mean and remove it from the set

Step 4 If the number of points left in the set is greater than a given size go back to step 1

Step 5 Use the mean as location estimate

Note that when the depth is unknown then the location can be obtained, using this method, at multiple depths and the final estimate can be chosen as the best depth based on the number of points left in the set for each depth.

Chapter 4

Results

4.1 Introduction

The previous chapter explained the experiments that were done in order to evaluate a variety of subspace tracking techniques for the discrimination of UXO in airborne magnetic field data. The results of these experiments are presented in this chapter, starting with an examination of the data and its principal components, which show that there is a subspace for the dipole's response. However, looking at the noise of the data in section 4.3, it is not spatially white as assumed by the two statistical subspace tracking techniques, namely Maximum Likelihood Estimation (section 2.3.4) and Geometric (section 2.3.5). This explains why the methods had poor or no convergence, as mentioned in section 3.6. The remaining sections of this chapter present the results for the SVD and ULV (sections 2.3.2 and 2.3.3) with a discussion of these results at the end of the chapter. The SVD method was applied as a filter by retaining one, two or three principal components, thus in most cases four set of results are shown, three for the SVD and one for the ULV. The methods were implemented on 10 sets of simulated data and in the results the dashed lines represents the 95% confidence intervals.

4.2 Data and Subspaces

The creation of the simulated data used for evaluating the subspace tracking methods is explained in section 3.4. Creating the simulated data required the use of measured background data for the earth's response and generated data for the dipole's response. An example of 6 recorded gradients, before rotation, used to create the simulated data is shown in figure 4.1. The data was sampled at approximately 0.1275 metres intervals. The simulated magnetic field gradients of a dipole, with the turbulence of the measured data's flight path, are displayed in figure 4.2. The data contains six channels all of which were used when compensating with the SVD and ULV decomposition. However the channel with the greatest amount of noise is removed when inverting as only five channels are independent (section 2.4.1). When decomposing the data using the SVD, it is clear that the first three principal components (eigenvectors of the data covariance matrix) are the three components of the total magnetic field, due to their high correlation, which is illustrated in figure 4.3. While in figure 4.4 it is shown that the fourth principal component is correlated to the magnitude of the simulated dipole. The significance of each of the principal components can be measured by its singular value, listed in table 4.1. It is evident that the significance of the dipole's response is three orders of magnitude less than that of the earth's, and that the dipole's signal to noise ratio is approximately 5:1 which is relatively high.

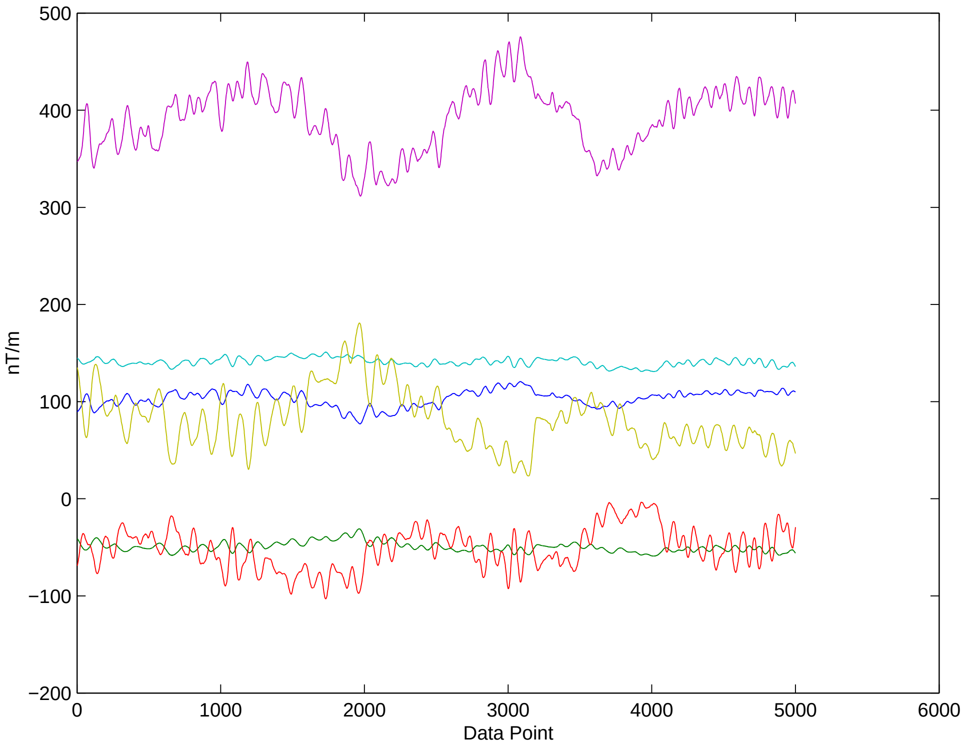

Figure 4.1: Measured data of the earth's magnetic field gradients.

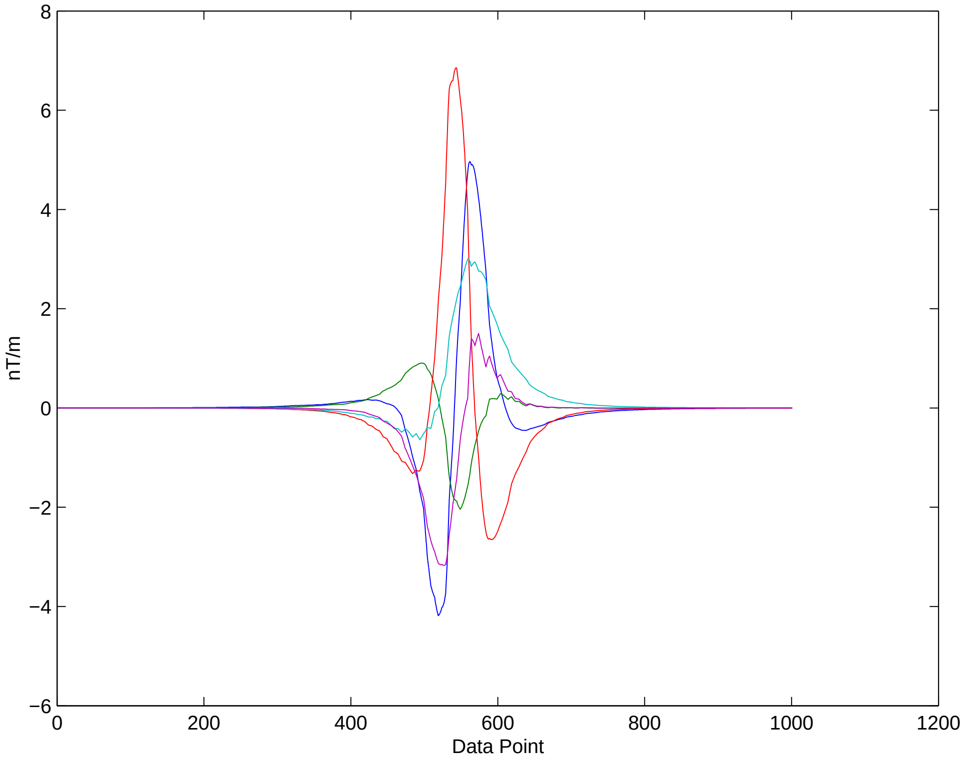

Figure 4.2: Magnetic field gradients for a simulated dipole.

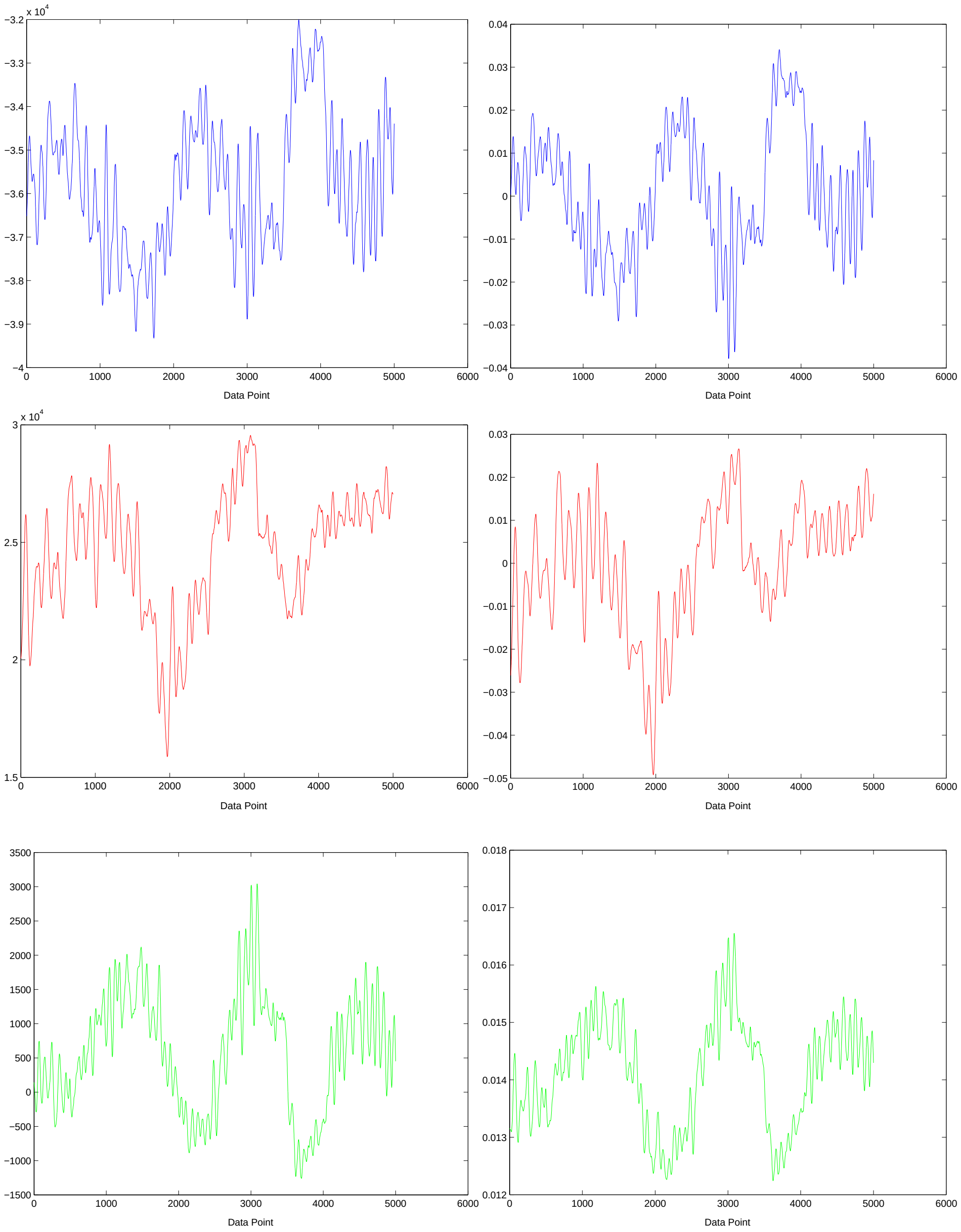

Figure 4.3: The total magnetic field values from the measured data (left) and the three most significant principal components of the simulated data (right).

Singular Value	Principal Component
31314.963510	Earth's magnetic moment (z-component)
2614.820997	Earth's magnetic moment (x-component)
1266.758058	Earth's magnetic moment (y-component)
55.049854	Magnitude of dipole's magnetic moment
24.261374	Additional dipole information
11.403705	Noise

Table 4.1: Singular values of SVD principal components.

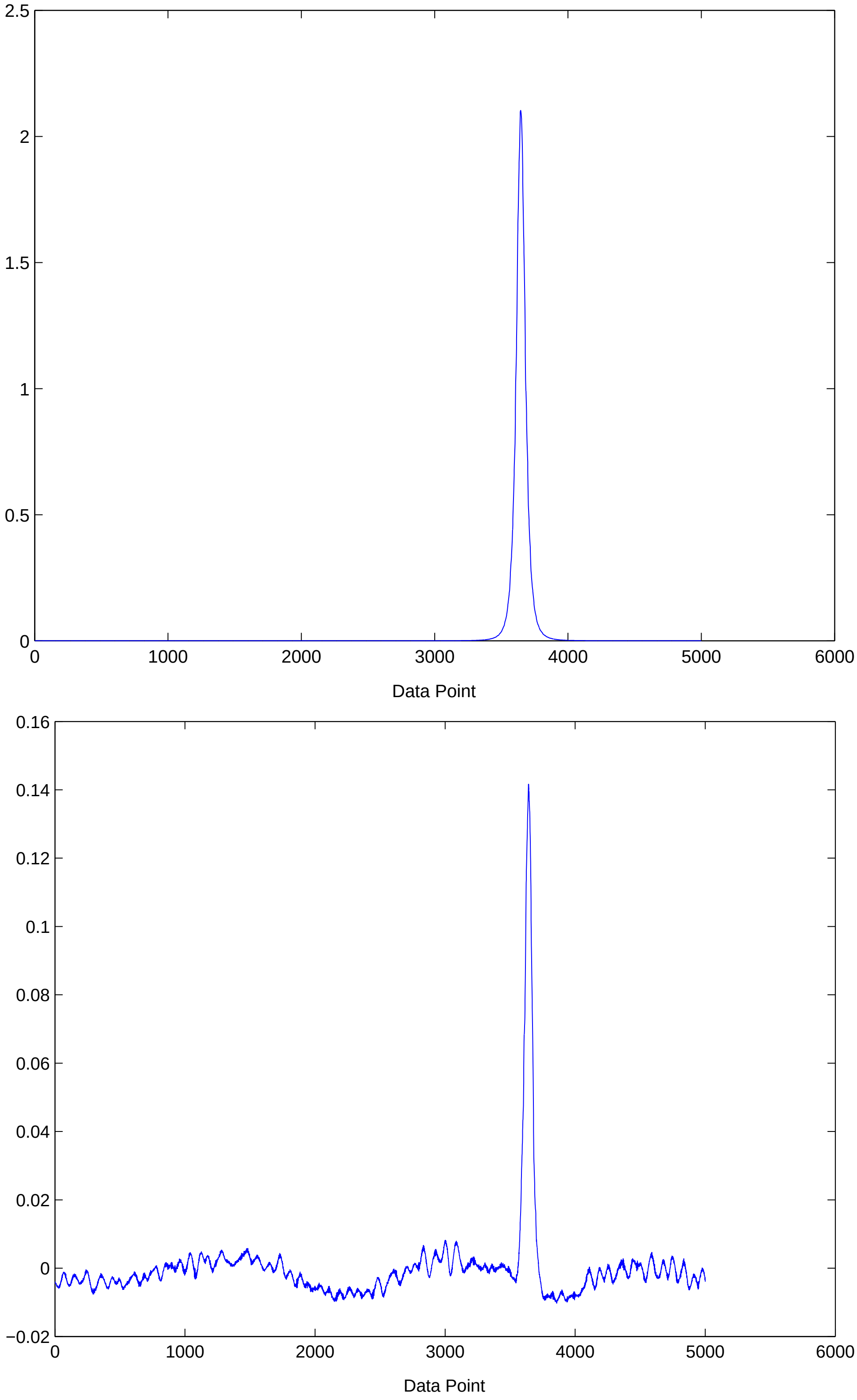

Figure 4.4: The true magnitude of the simulated dipole (top) and the fourth principal component.

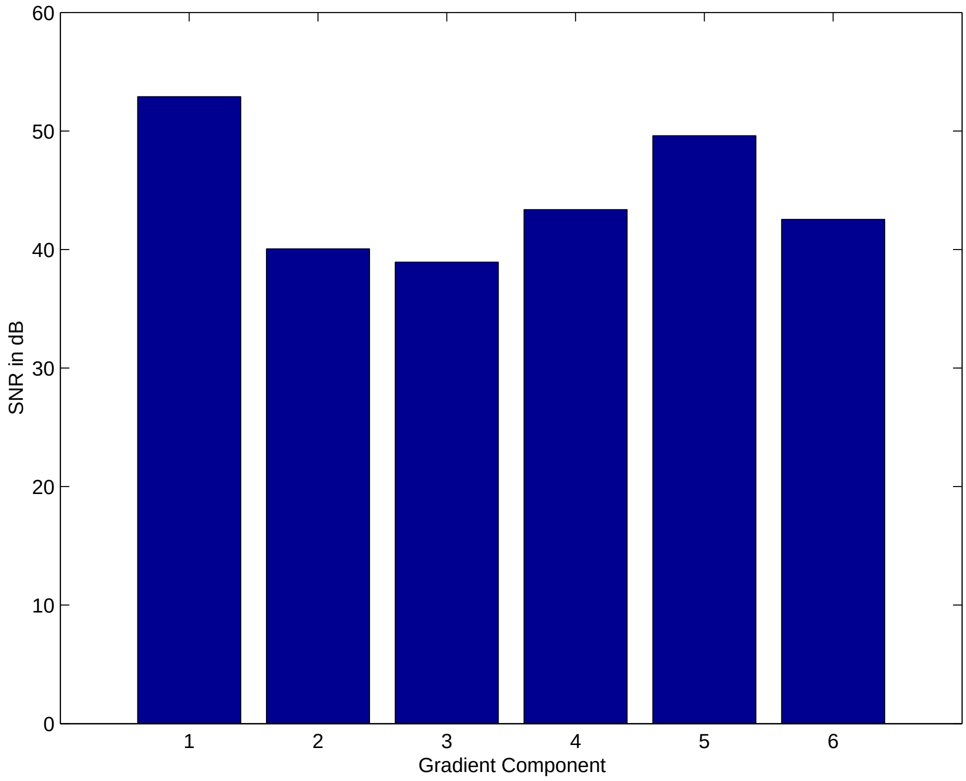

Figure 4.5: Background SNR.

4.3 Signal to Noise

The statistical subspace tracking techniques applied, namely MLE (section 2.3.4) and Bayesian Geometric (section 2.3.5), make assumption about the structure of the noise in the data, thus an analysis of the noise and the signal to noise ratios (SNR) was done. This analysis assumed a linear Gaussian noise model and using the EM (expectation maximization) algorithm was used to calculate the SNR and noise variance, as in [21]. The SNR for the background signal (measured data) is given in figure (4.5) with the noisiest SNR, component 3, at 38.94 dB which is a ratio of approximately 7827:1. The mean source signal (simulated dipole) SNR, as shown in figure (4.6), is around three orders of magnitude lower than the background, with a highest ratio of about 383:1 (25.83 dB). The noise variance, which is presented in figure (4.7), differs greatly between the different channels. This is clearly not spatially white noise (it is not independent and identically distributed) as assumed by the statistical methods and with the lowest mean source SNR ratio at 5.4:1, the noise assumptions are very relevant. Further more the high levels of noise make the estimation of σ very important. If σ is to larger the source is included as noise and to small leads to extra noise in the signal. Due to these problems the statistical methods diverged or had very slow convergence with results that were out by up to five orders of magnitude. Thus these result are not shown and only the results from the other methods are discussed in the rest of this chapter.

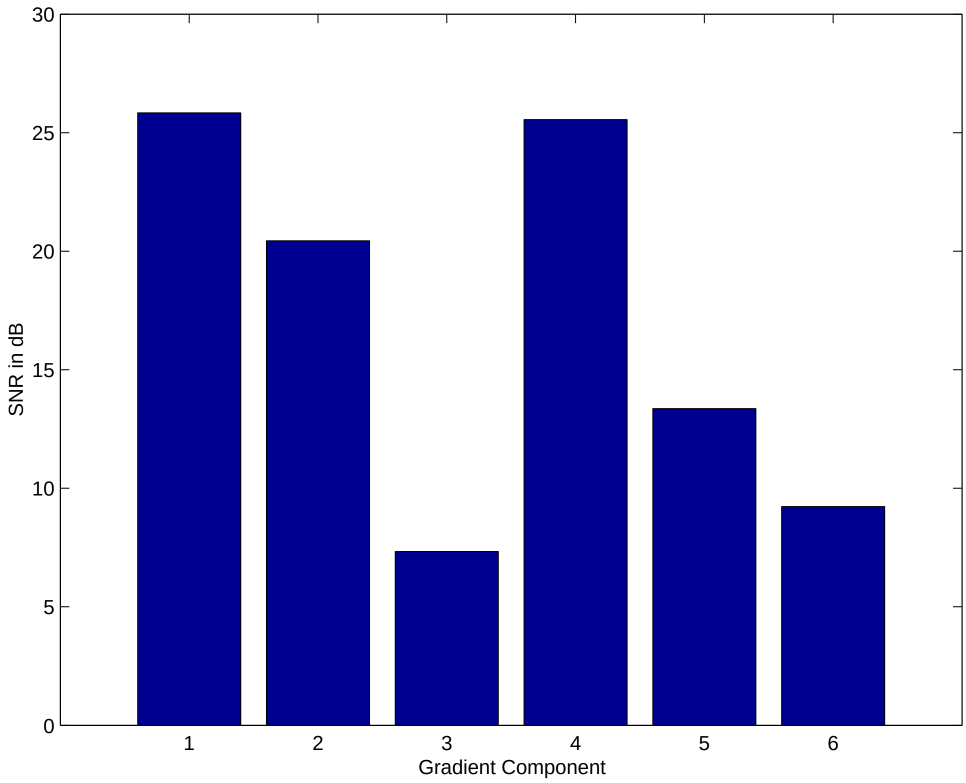

Figure 4.6: Source SNR.

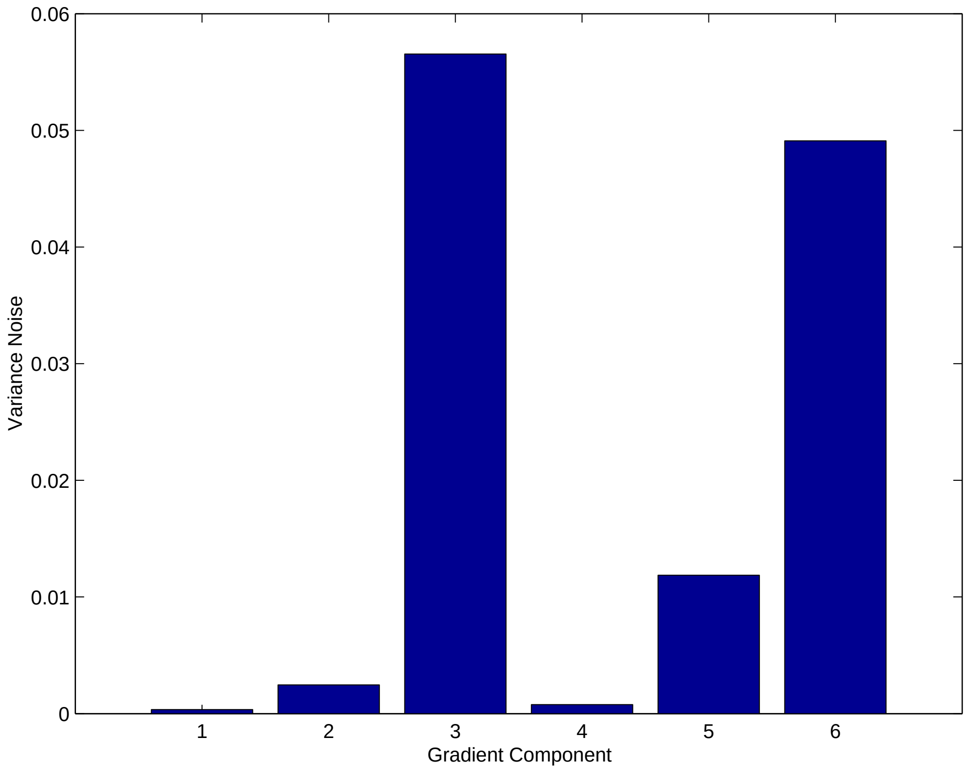

Figure 4.7: Variance of Noise.

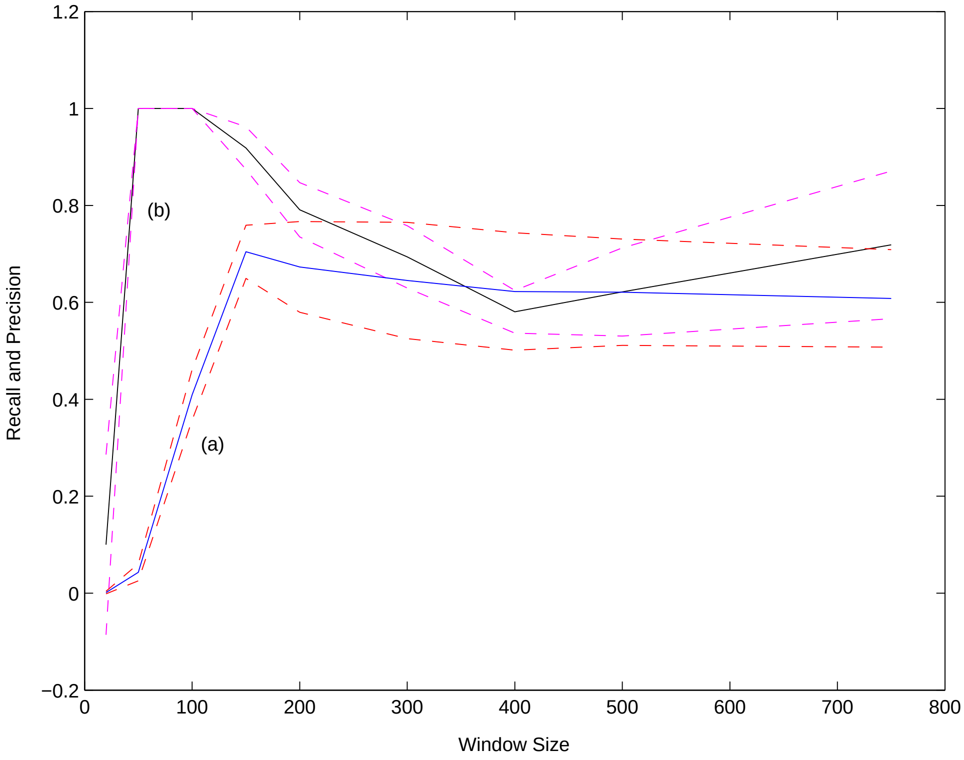

Figure 4.8: (a) Recall and (b) Precision of classification using one principal component of the singular value decomposition, with a 95% confidence interval.

4.4 Recall and Precision

Figures (4.8) - (4.11) show the recall and precision of the classification after filtering the data with the three singular value decompositions (SVD), namely one, two and three principal component, and the ULV decomposition. The recall of a classification is the number of correctly classified points from the class of interest (i.e. dipoles) divided by the total number of points of that class. The precision is the number of correctly classified points from the class of interest divided by the total number of points that have been classified as coming from that class. It can be seen, from figures (4.8) - (4.10), that the precision of the SVD methods is best for the window sizes of 50 and 100 data points. Here the precision is 1, meaning that all the classified points were if fact points of interest, but the recall was rather low here so for these window sizes only a few points very close to the maximum response from the dipole are showing any sign of it. Windows sizes of 20 or less data points have zero recall and although recall continues to increase as the window size gets greater than 100 the precision decreases, as can be expected, the greater recall is due to more classifications, since more data makes it easier to decompose the earth's response from that of the dipole, but there is also an increases in the number of incorrect classifications. The ULV method had a recall of 1 for all the window sizes in the experiments and so only the precision is shown, in figure (4.11), and this was very low for all window sizes. This is not ideal but the total recall means that all of the true data points are included in the classification and the number of misclassified points should be reduced by the estimation algorithm, when removing the outliers.

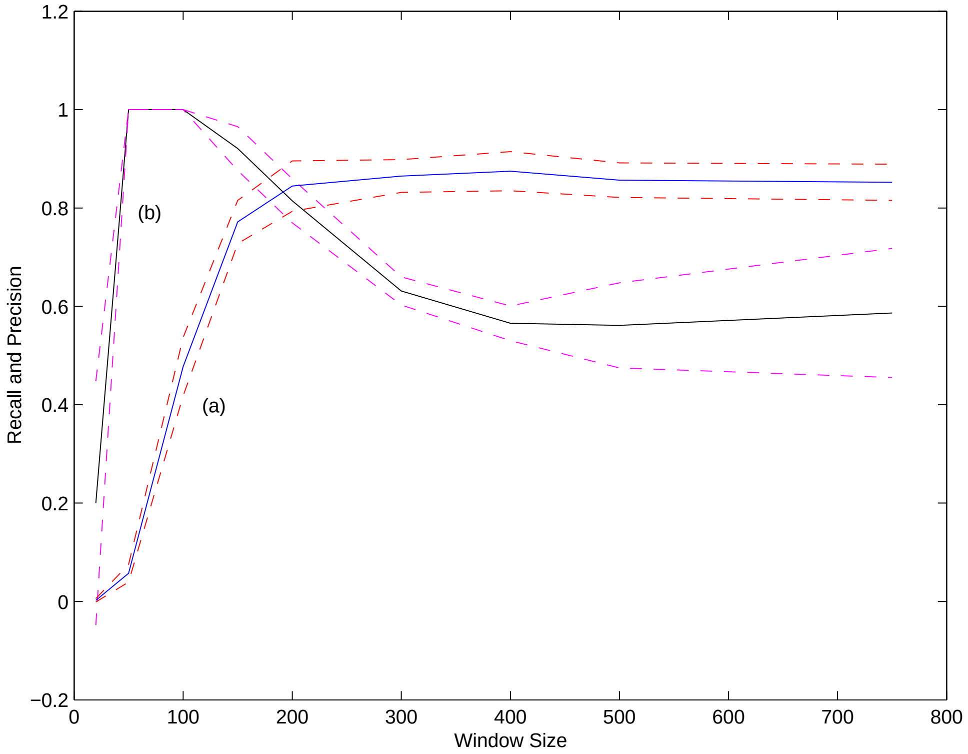

Figure 4.9: (a) Recall and (b) Precision of classification using two principal components of the singular value decomposition, with a 95% confidence interval.

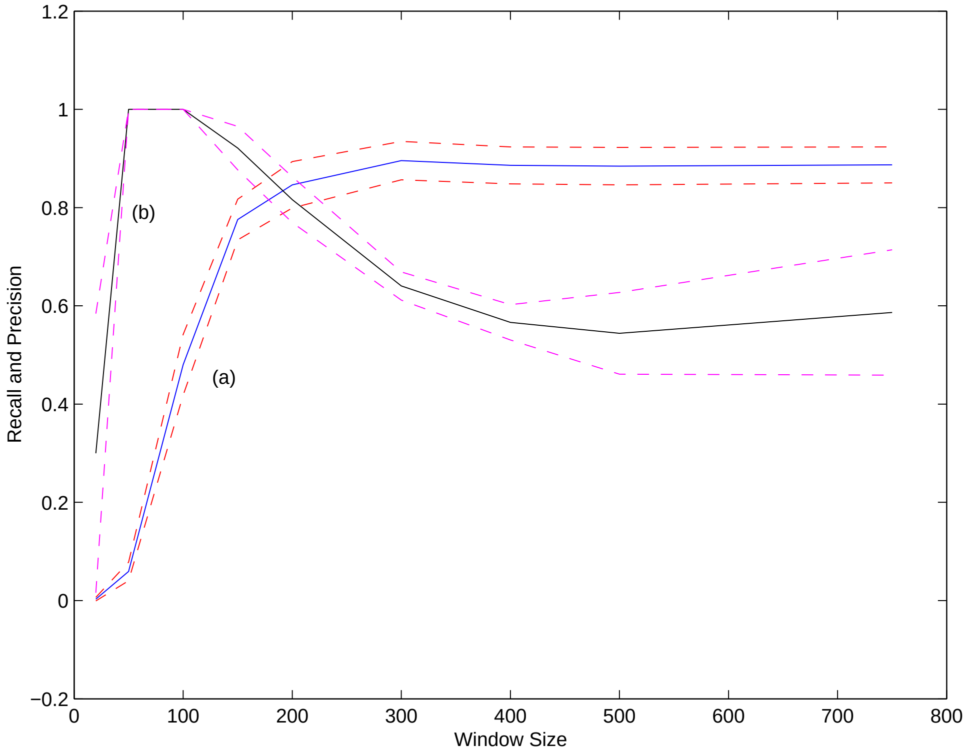

Figure 4.10: (a) Recall and (b) Precision of classification using three principal components of the singular value decomposition, with a 95% confidence interval.

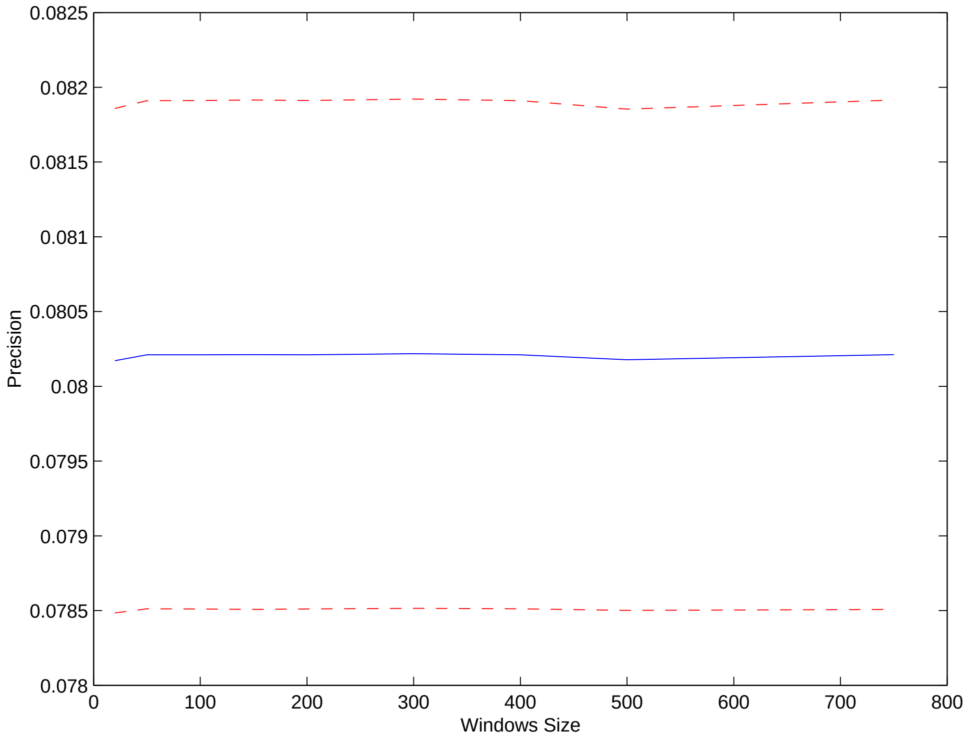

Figure 4.11: Precision of classification using the ULV decomposition, with a 95% confidence interval (Recall is 1 for all window sizes).

4.5 Estimation Errors

The error in the location estimation of the dipole for the four orthogonal-subspace filtering methods, shown in figures (4.12) - (4.15), is the Euclidian distance from the estimate to the true location. The SVD methods all have there best results with a window size of 150 where the errors are approximately between 3.5 and 4 metres. Even though it had very low precision (as discussed in the previous section) the ULV method produced better estimates with errors of just over 3 metres with most windows size greater than 150). The estimation for the magnetic moment was highly inaccurate. These estimation errors are not shown but some indication of these results can be seen in section 4.8 where the errors in the inverted data are presented.

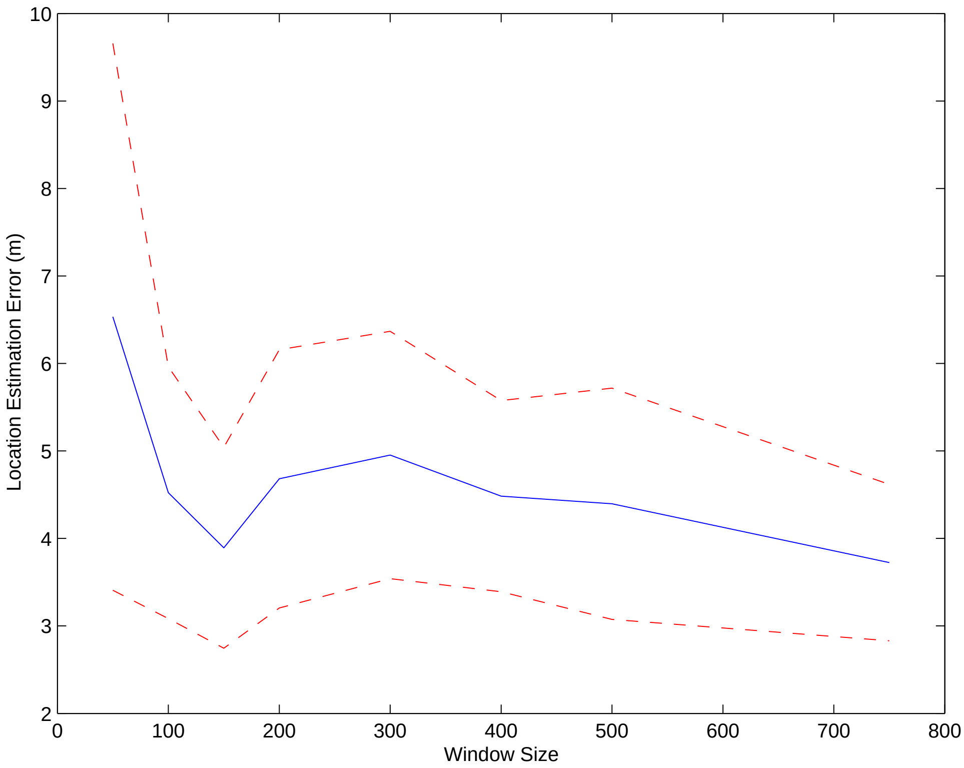

Figure 4.12: Error in location estimation using one principal component of the singular value decomposition, with a 95% confidence interval.

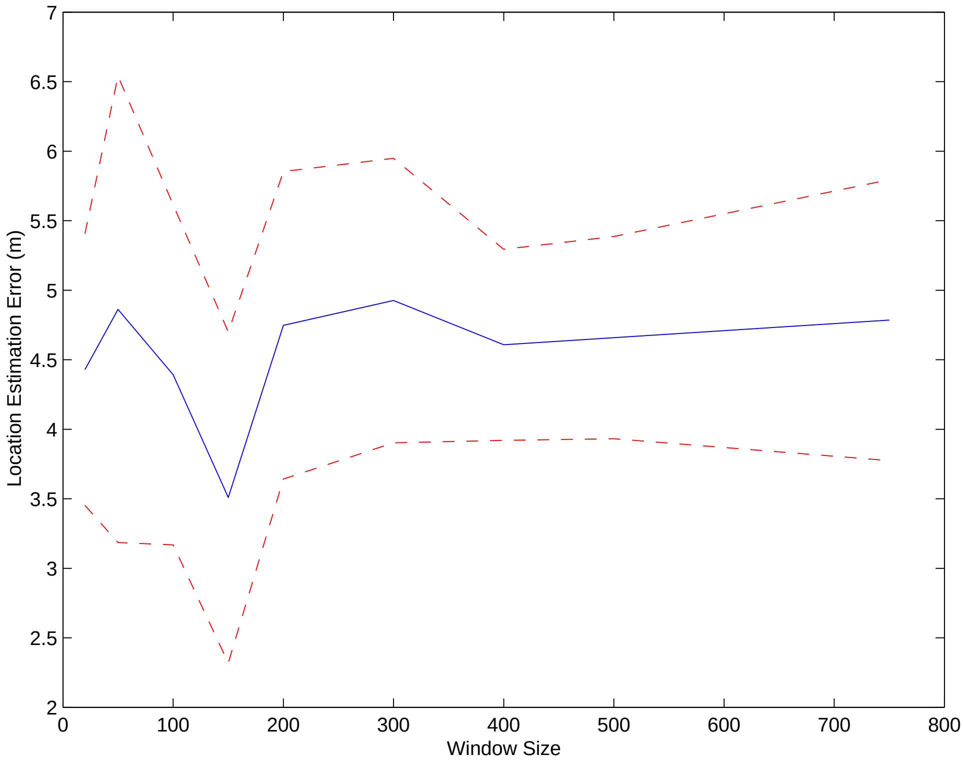

Figure 4.13: Error in location estimation using two principal components of the singular value decomposition, with a 95% confidence interval.

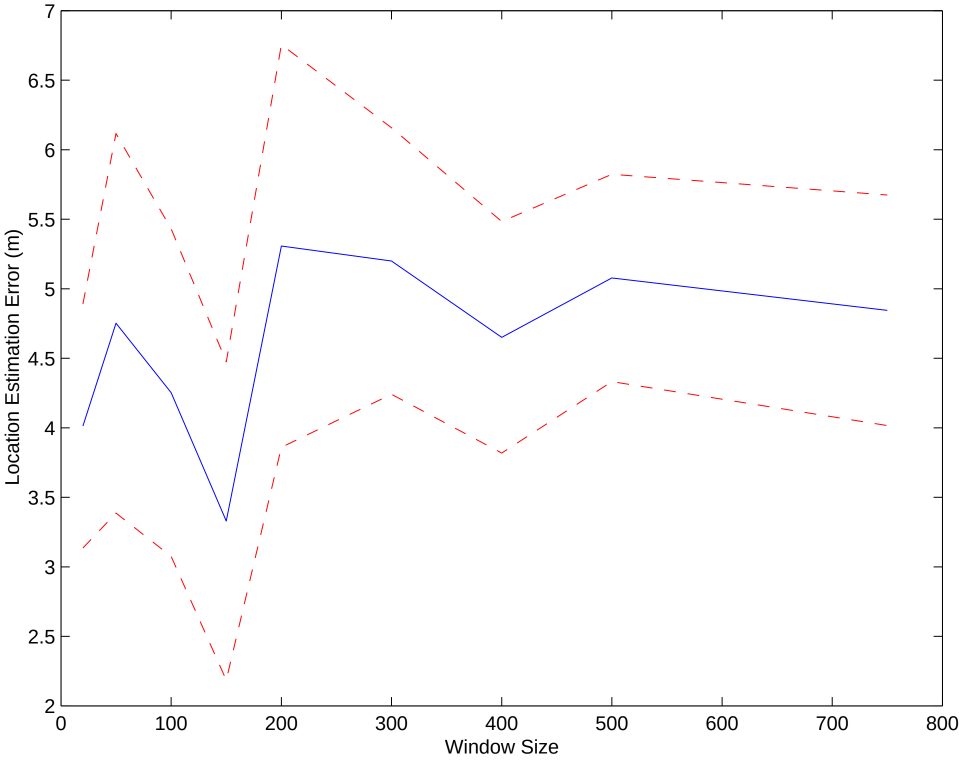

Figure 4.14: Error in location estimation using three principal components of the singular value decomposition, with a 95% confidence interval.

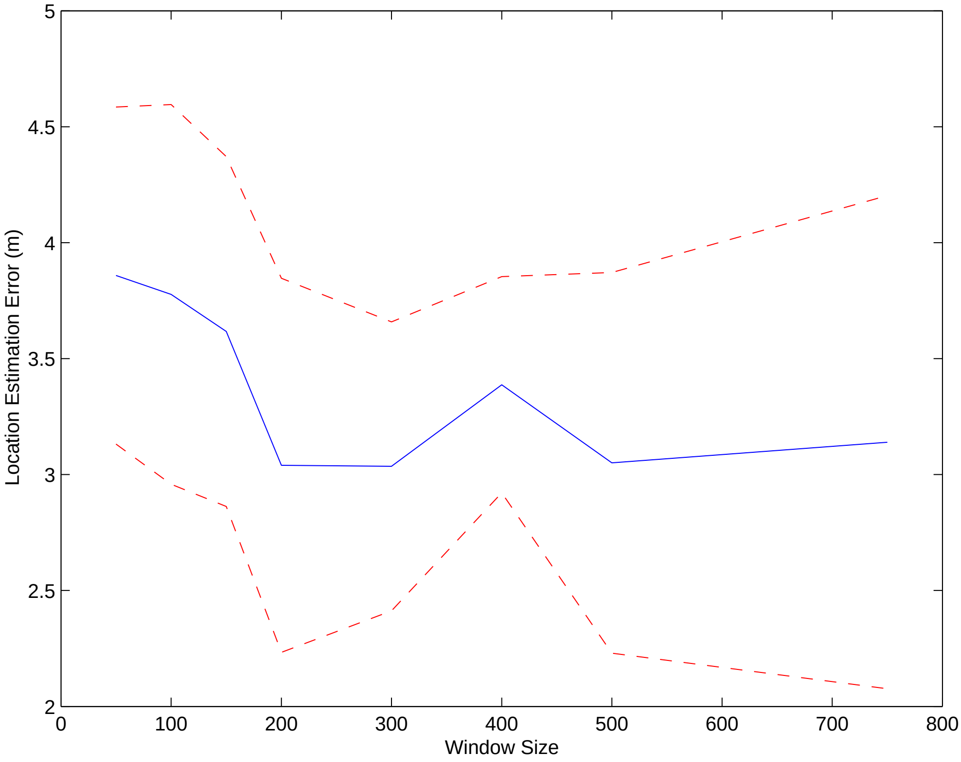

Figure 4.15: Error in location estimation using the ULV decomposition, with a 95% confidence interval.

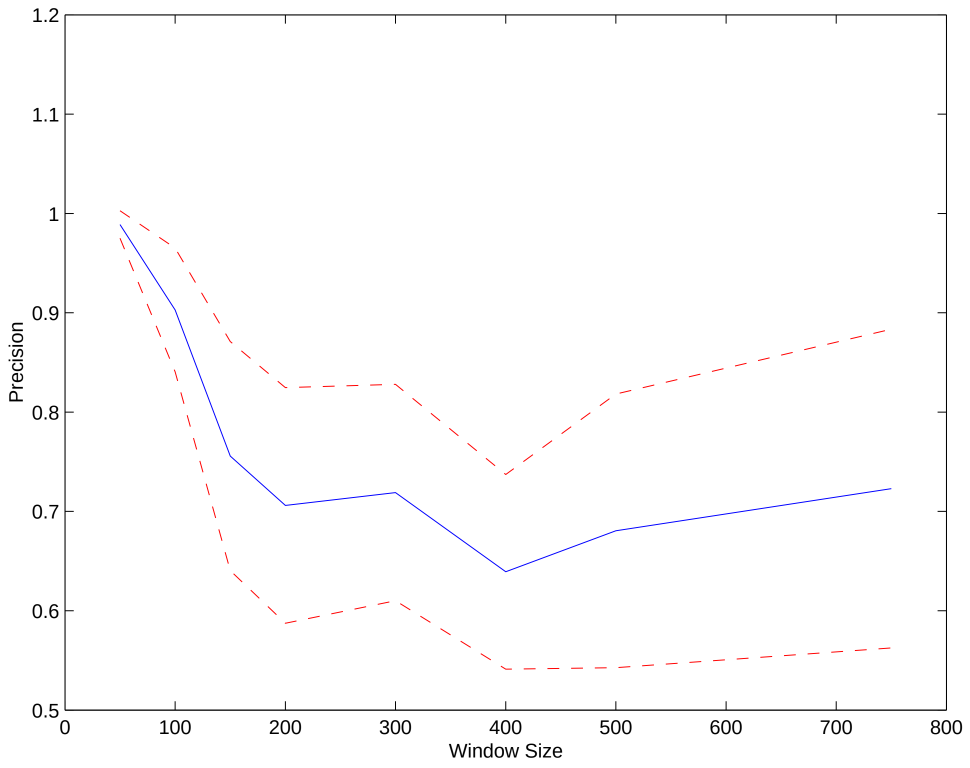

Figure 4.16: Precision of estimation cluster using one principal component of the singular value decomposition, with a 95% confidence interval.

4.6 Cluster Precision

The estimation algorithm described in section 3.7 suggested that a possible method for obtaining a depth estimate, when the true depth is unknown, is the depth with the greatest number of points in it's final cluster. Alternatively the percentage of the classified points in the final cluster (precision of the cluster) can be used, since this allows a better measure for comparison when performing multiple tests. These precision values for the four methods, at the known depth of the dipole, can be seen from figures (4.16) - (4.19). With the SVD methods, the cluster has a high precision for the 50 and 100 data point window sizes where the initial recall of the classification was very low. Thus there are very few intersection points and, since the precision of the initial classification was high, there are hardly any outliers. As the window sizes increase the precision of the cluster drops and then picks up similarly to the precision of the classification, this relation suggests that the majority of the final cluster for the estimation are correctly classified points. In the case of the ULV decomposition the precision of the clusters are greater than the precision of classifications. With the total recall of the classification and very low precision, it is most likely that all the points near the correctly classified points are also classified and so these misclassified point are also with in the cluster.

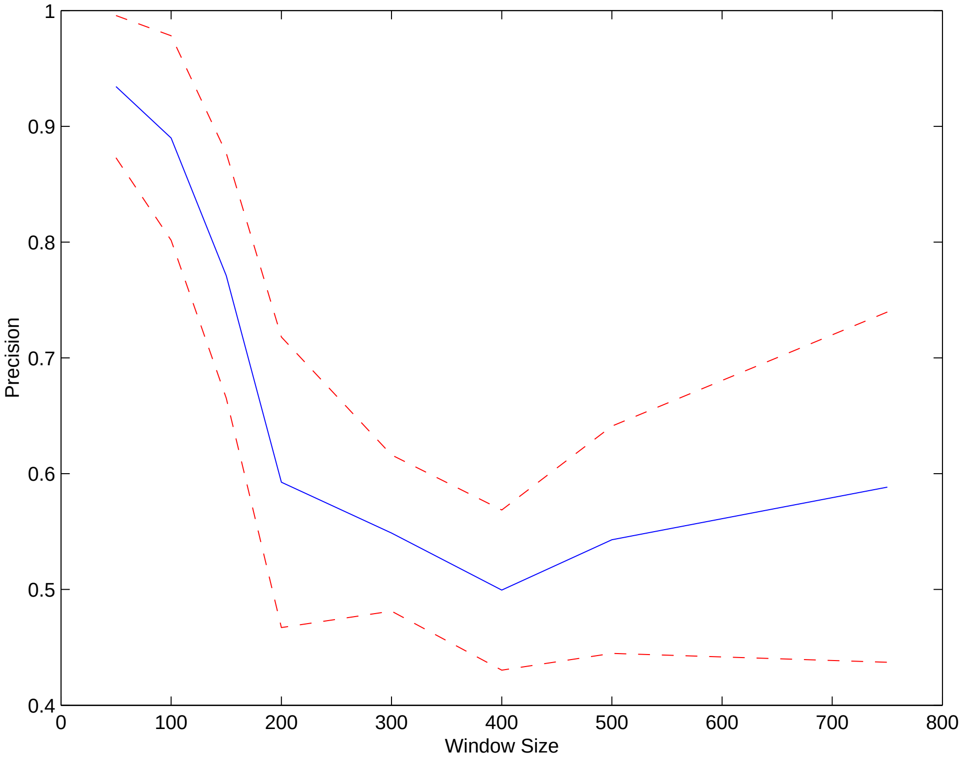

Figure 4.17: Precision of estimation cluster using two principal components of the singular value decomposition, with a 95% confidence interval.

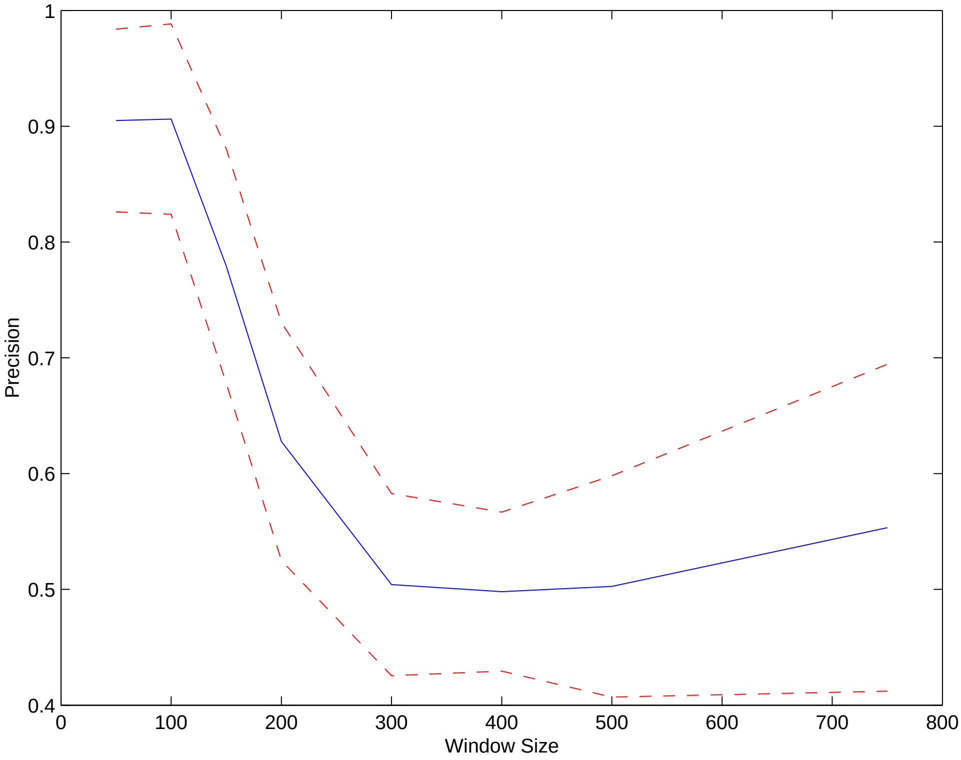

Figure 4.18: Precision of estimation cluster using three principal components of the singular value decomposition, with a 95% confidence interval.

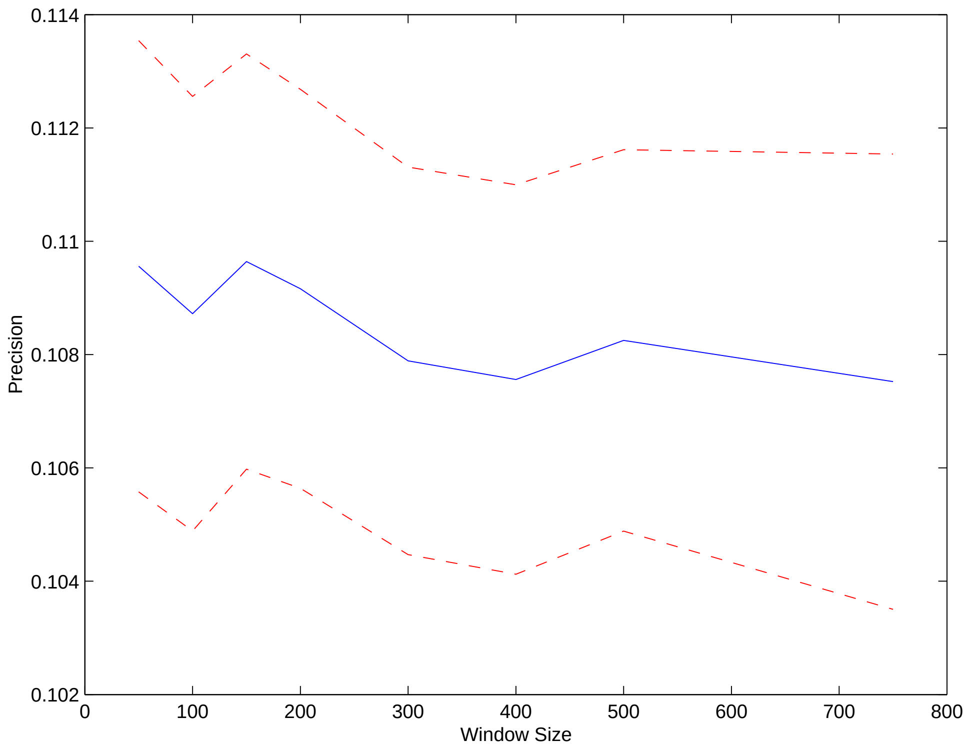

Figure 4.19: Precision of estimation cluster using the ULV decomposition, with a 95% confidence interval.

4.7 Filter Correlation

The correlation of the data which has been filtered using the SVD methods with various window sizes, centered at the peak of the dipole's magnitude, with the simulated data of the dipole is shown in figure (4.20). The correlation improves as the windows gets bigger but seems to level at around 0.5 for the three principal component filter, which is the best case. However, this is not a significantly high correlation.

4.8 Errors in angles of r and m

Figure (4.21) shows the mean angular error, in degrees, of the vector **r** (the directions to the dipole) over the correctly classified points, with a 95% confidence interval (the number of correctly classified points was generally over 100). The error decreases as the window size increases but is always rather large. The mean angular error for the vector **m** (direction of the magnetic moment) is shown, with 95% confidence interval, in figure (4.22). The estimation of the magnetic moments is almost perpendicular to the true moment. It is clear from the size of the errors that both the direction vectors to the dipole and the magnetic moment vectors are incorrect and that the filtering process is inaccurate (as can be seen by the low correlation mentioned in the previous section). The filter inaccuracy explains the poor estimates of the magnetic moment. However the estimates of the dipole location was not as poor as these errors suggest.

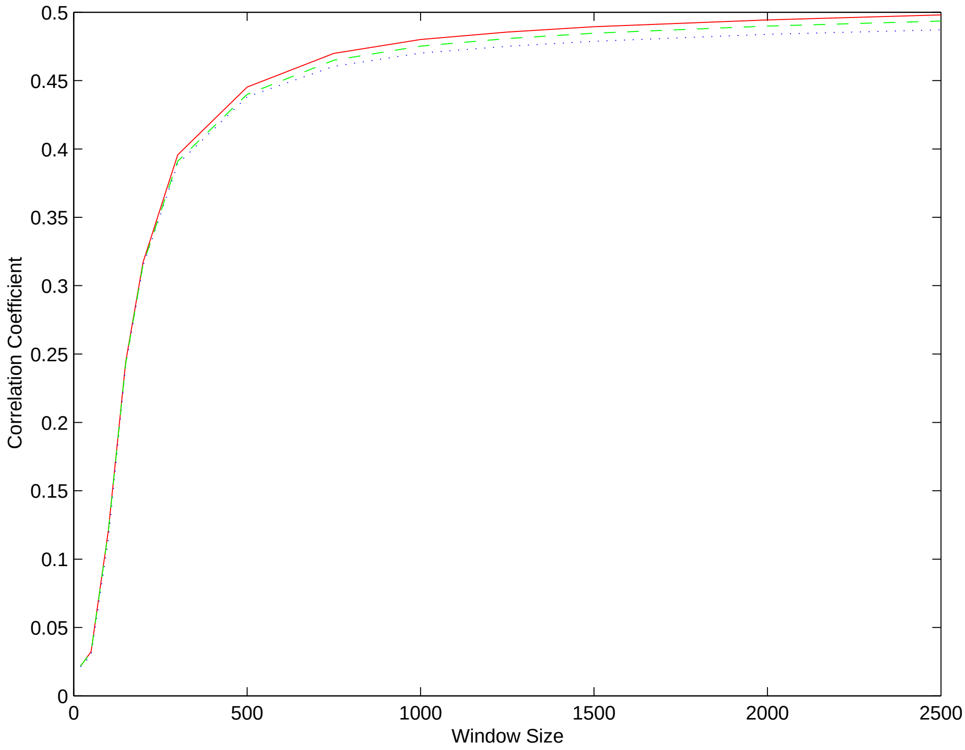

Figure 4.20: Correlation of SVD filtered data, with one (· · ·), two (- - -) and three (—) principal components, to true magnetic gradients.

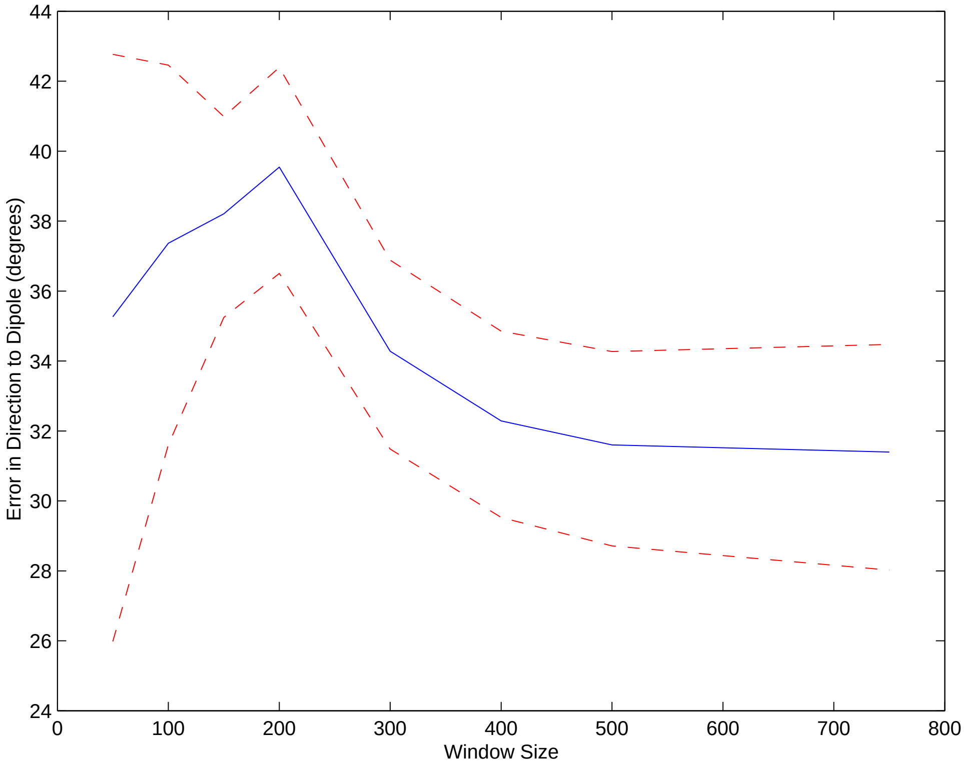

Figure 4.21: Mean inversion error of the direction to the dipole, **r**, in degrees from the true direction, with a 95% confidence interval.

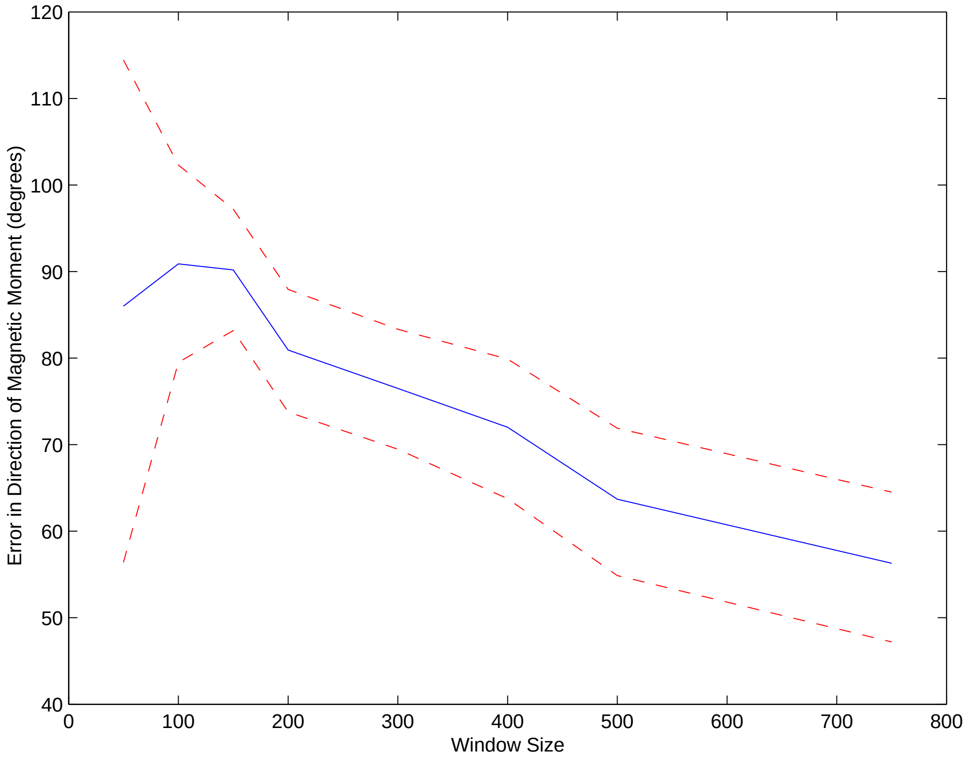

Figure 4.22: Mean inversion error of the magnetic moment's orientation, **m**, in degrees from the true orientation, with a 95% confidence interval.

4.9 Cluster

The estimate of the dipole location is not the direct result of the inversion but also the removal of outliers, as described in section 3.7. Figure 4.23 illustrates the cluster of points, for a test with the SVD method using two principal component and a window size of 150. The angular errors in the inversion are clear from the scattering of the points (top) but after the outliers are removed (bottom) only the points in the middle close to the true location (star) are left and are then used for the estimated location (triangle). The square, on the flight path in the bottom plot, is the sensor location for which the dipole response subspace, relative magnitude of the magnetic moment, is greatest when decomposing with the SVD over the full data (window size of 5000). Figure 4.24 is an example of the intersection points for the ULV method and shows how they just follow close to the flight path with the most dense area being close to the true location. This area has a greater weight during the removal of outlier and remains as the final cluster for the estimate.

4.10 ULV Decomposition

The ULV Decomposition over a large section of data does produce a high correlation between the three strongest subspaces and the measured total field responses and an isolated peak does appear in the other subspaces. However, after recomposing the data with the three most significant subspaces set to zero there is almost always sufficient magnetic energy in this data for the magnitude of magnetic moment from the Frahm inversion to be greater than the tolerance for classification as a dipole response. This is unlikely to be due to the noise and thus must be

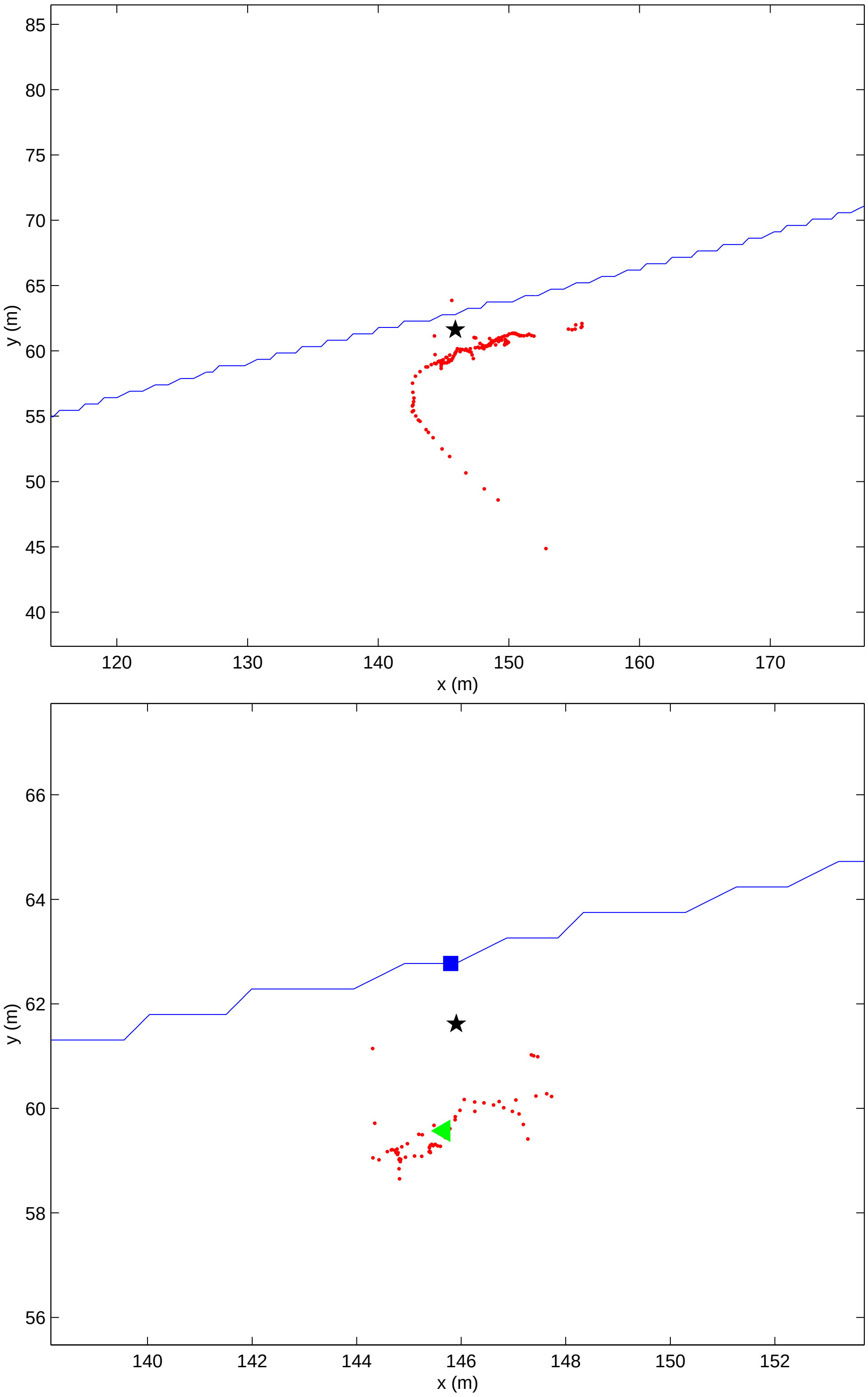

Figure 4.23: The flight path and points of intersect between the direction vectors (SVD) and ground level before (top) and after (bottom) the removal of outliers. The true location is shown by the star, while the triangle is the location estimated by the inversion and the square is the maximum response of the magnitude of the magnetic moment.

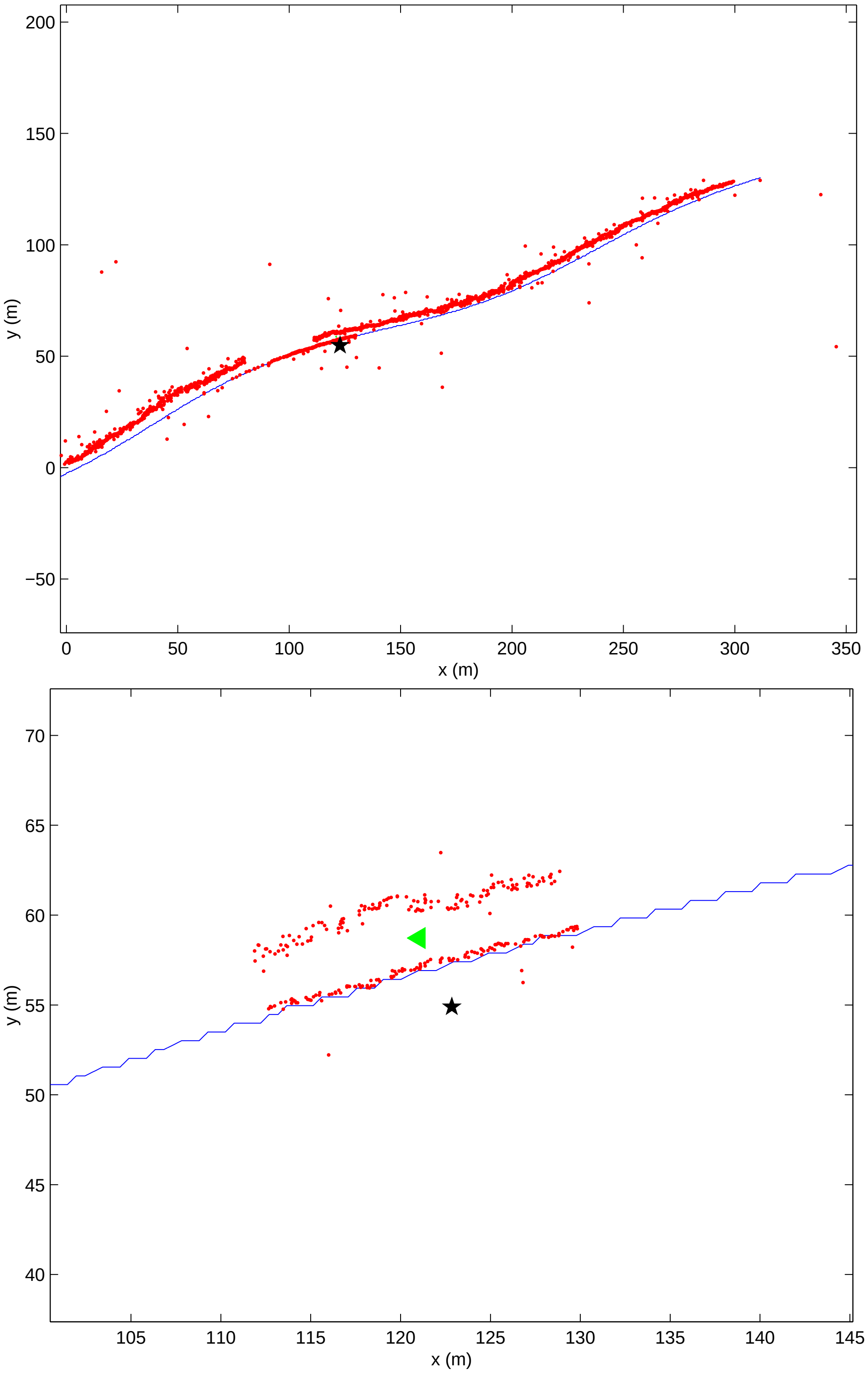

Figure 4.24: The flight path and points of intersect between the direction vectors (ULV) and ground level before (top) and after (bottom) the removal of outliers. The true location is shown by the star, while the triangle is the location estimated by the inversion and the square is the maximum response of the magnitude of the magnetic moment.

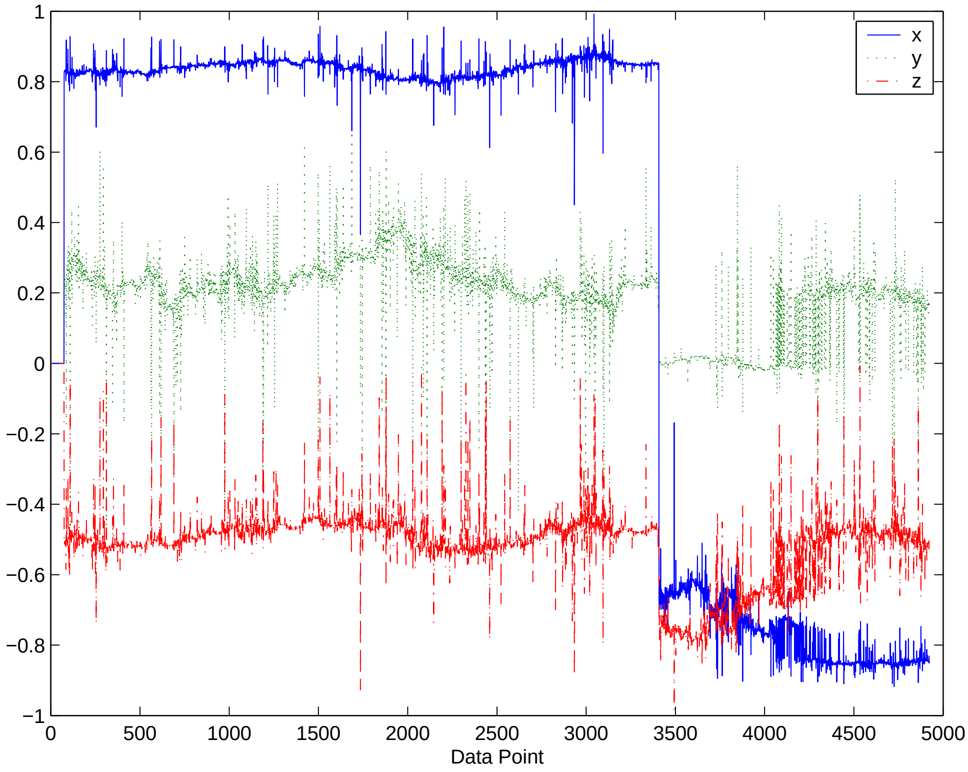

Figure 4.25: Direction to the dipole, **r**, after ULV filtering, with a window size of 150.

from the earth's magnetic field. The earth is below the sensor and so it can be expected that the direction vector, **r** shown in figure 4.25, will be downward and the intersects with the ground will be close to below the flight path, as seen in figure 4.24. Note, in figure 4.25 the x-axis is inline with the flight path and positive forwards, the y-axis is positive to the left and the z-axis is positive upwards. Also the ambiguities of the Frahm inversion were resolved by using the vector closest to the true solution, rather than the deepest solution, as this gives a clearer graph but still shows that the results are always downwards.

4.11 Frahm Inversion

In section 4.9 it was illustrated that the clusters of points were well spread. This is most likely the result of the poor filtering (section 4.7) but the effect of noise on the inversion could also be a factor. A simulated dipole was created without any recorded data being added for the earth. The inversion was then tested on this gradient data with different levels of added noise. With no added noise the cluster is a single point at the true location as seen in figure (4.26). Figures (4.27) and (4.28) show the clusters for the same dipole after adding zero-mean independent and identically distributed Gaussian noise with variances of 0.005 (SNR of approximately 12dB) and 0.05 (SNR of approximately 8dB) respectively. With the SNR at 12dB the clustering is very good and although it does spread when the SNR is 8dB the outliers are well centered around the true location which has a dense cluster of points.

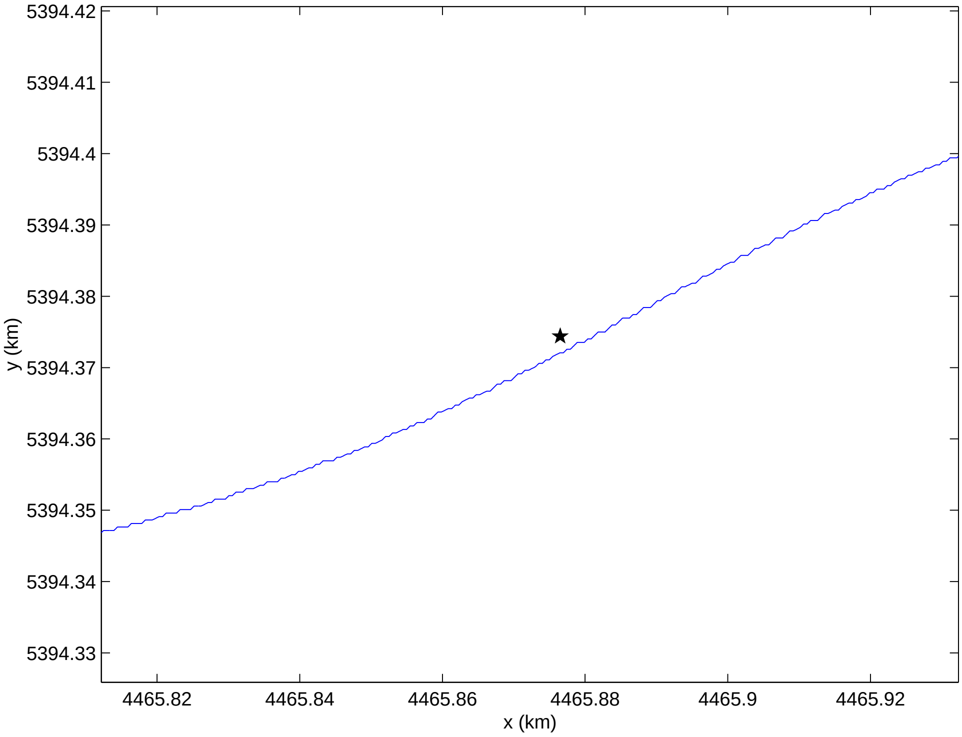

Figure 4.26: Point of intersect for the Frahm inversion on a simulated dipole with no noise.

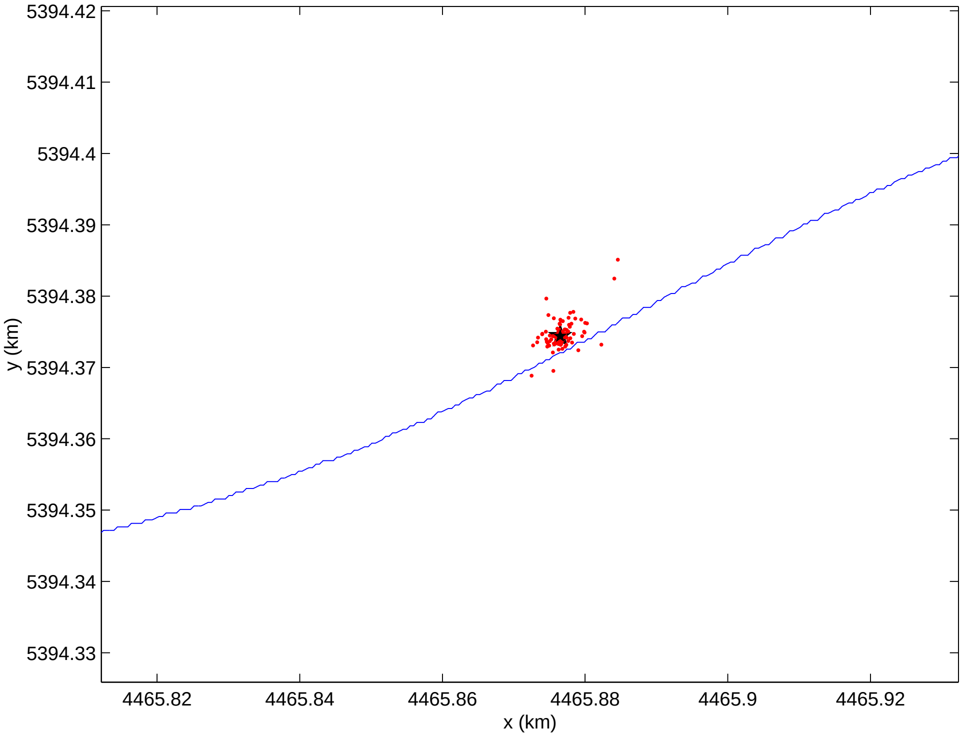

Figure 4.27: Points of intersect for the Frahm inversion on a simulated dipole with added noise at a SNR of 12dB.

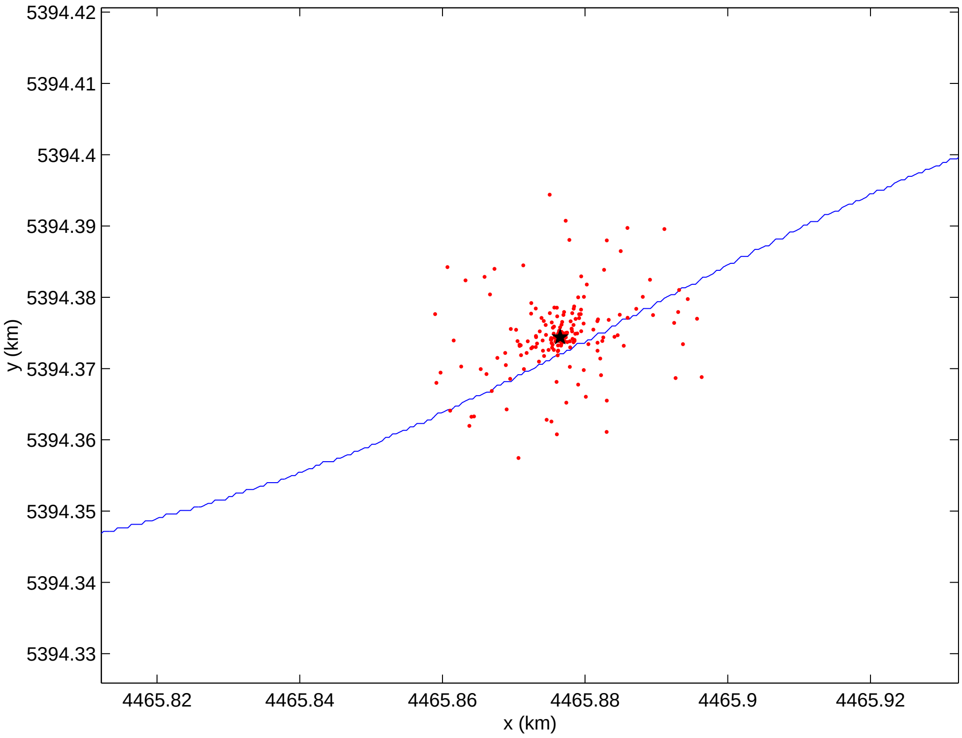

Figure 4.28: Points of intersect for the Frahm inversion on a simulated dipole with added noise at a SNR of 8dB.

4.12 Euler Deconvolution

Due to the poor results with the Frahm inversion, which only uses the one (center) data point of each filtered window, some testing was done with the Euler deconvolution. The Euler deconvolution uses a window of data to estimate the location of the anomaly and has been applied to locating UXO [7] using total magnetic field data were the gradients had to be estimated. When the Euler deconvolution was applied to the gradient data the results were less accurate than those of the Frahm inversion. One possible problem is that the test data used for this research has a single line flight path and the method should work better with grid data, as was applied in the total magnetic field experiment [7].

4.13 Discussion

The high correlation between the principal components (using SVD over the full data window) with the three components of earth's magnetic field and the magnitude of the dipole (section 4.2), suggests that subspace tracking can be used to discriminate the dipole from the earth's response. However, the correlation of the filtered data with the simulated dipole was at best 0.5 (section 4.7). In the case of the small window sizes this is possibly due to insufficient data for the relatively high noise level. With the large windows it is probably due to the assumption that the flight path is stationary over the length of the window. These low correlations suggest that the inversion will not be accurate and explains the poor results for the estimation of the magnetic moment. The estimation of the dipole location seemed reasonable, but this was not due to accurate inversion as can be seen from sections 4.8 and 4.9. The direction vectors were not accurate and had large variations. The use of the deepest solution for removing the ambiguities in the Frahm inversion insures that the position vectors are close to downward and this coupled with the low altitude of the the flight path would lead to clusters of points, on the ground, close to the areas of dense classification. The estimation algorithm then removes the outlying points and is left with a cluster around the area of the dipole.

Chapter 5

Conclusion

The research was an investigation into the use of subspace tracking methods for the discrimination of unexploded ordinances (UXO) in airborne magnetic field gradients. This involved experimentation, on simulated data, with four subspace tracking techniques. The SVD (section 2.3.2) and the ULV (section 2.3.3) are algebraic techniques which produce orthogonal subspaces. The three components of the magnetic moment are not independent. Thus the orthogonal subspaces cannot separate these components and so the techniques can be used to filter the data but further processing is needed to find the final solution. This inversion was done using Frahm's method (section 2.4.2). The statistical techniques, MLE (section 2.3.4) and Bayesian geometric (section 2.3.5), use a defined direction matrix (section 3.6) and estimate the parameters, so no further inversion is required. Unfortunately, the statistical techniques had slow or no convergence. Even when there was convergence the results were very inaccurate. The experimentation was done on simulated data, created using measured data for the earth's magnetic field and a synthesized dipole response (section 3.4). After the data had been filtered and inverted, each data point was classified as a dipole or not based on the magnitude of the inverted magnetic moment. The classified points were then used to estimate the dipole's location and moment by eliminating outliers and taking the mean of the remaining cluster (section 3.7). The results of the experiments were presented in the previous chapter. The discussion of the results, in section 4.13, suggests that the poor results are due to the high noise level relative to the dipole source and the averaging of measurement location over the window. The reasonable location results were from the estimation removing outliers and then taking the mean of the cluster which was close to the dipole because of the low altitude of the sensor and high density of classified points close to the dipole. Although subspace tracking proved ineffective at finding an accurate estimate of the dipole, it (in the cases of the SVD) does provide a good result for the magnitude of the magnetic moment. Since the magnetic field response is inversely proportional to the cube of the distance from the dipole it is safe to assume that the peak magnitude of the measured magnetic response is the closest point to the dipole along the flight path, as in figure 4.23. Thus an estimate for the location can be given as below the peak or in the plane orthogonal to the flight path at that point. If a grid survey is carried out, a mesh of the magnitudes can be created and the peaks used to estimate the location of dipoles. Although this would not provide the magnetic moment to add in classifying the dipoles, it would still provide a useful map of the magnetic disturbances (possible landmines) in an area. It must be noted that in creating such a map, correction of the magnitude must be made for changes in the altitude of the fight path, as a low path to the side of a dipole can be closer than a high path directly above the dipole and thus would show a greater magnitude. Additionally, such correction would allow for the comparison of the different dipoles in the area and thus some classification based on known dipoles in the area (or from a library). The magnitude is not only effected by the distance but also by the true magnitude of the moment and its orientation and so some information could possible be gained from any axis of symmetry and/or the skewness of the dipole response and comparisons to dipoles with known magnitude.

Appendix

Matlab$^{\circledR}$ Code

Magnetic Field Gradients

```
function G = fwdeq(m,r)

% input m is the magnetic moment of the dipole, input r is the
% directional vector from the dipole to the field point and
% output G is the 5 independent magnetic field gradients at
% the field point

lr = sqrt(dot(r,r));

n = r/lr;

for j = 1:2
    for k = j:3
        H(j,k) = (3/lr^4)*(m(1)*Nijk(n,1,j,k)
            + m(2)*Nijk(n,2,j,k) + m(3)*Nijk(n,3,j,k));
    end;
end;

G = [H(1,1) H(1,2) H(1,3) H(2,2) H(2,3)];

-----------------------------------
function N = Nijk(n,i,j,k)

% Calculates the symmetric third rank tenor
% for the unit direction vector n

N = 5*n(i)*n(j)*n(k)
    - (kron_delta(k,i)*n(j) + kron_delta(k,j)*n(i)
         + kron_delta(j,i)*n(k));

-----------------------------------
function k_delta = kron_delta(i,j);

% Returns Kronica delta for input i,j
if i == j
    k_delta = 1;
else
    k_delta = 0;
end;
```

Frahm Inversion

```
function [r,m]=frahm(g)

% input g contains the magnetic field gradient components
% [Gxx Gxy Gxz Gyx Gyy Gyz Gzx Gzy Gzz]
% output r is the estimated bearing vector
% output m is the estimated magnetization vector

A=reshape(g,3,3);
[v,e]=eig(A);
e=diag(e);

s1=sqrt((a-b)/a);
s3=sqrt(b/a);
r=v*[s1 s1 -s1 -s1; 0 0 0 0; s3 -s3 s3 -s3]; % bearing vectors
s1=(5*b-a)*sqrt((a-b)/a)/3;
s3=(5*b-4*a)*sqrt(b/a)/3;
m=v*[s1 s1 -s1 -s1; 0 0 0 0; s3 -s3 s3 -s3]; % magnetic moments

k=find(r(3,:)==min(r(3,:))); % choose deepest solution
r=r(:,k)’;
m=m(:,k)’;
```

Simulated Data

```
function [Sim_G,r,m,di_x,di_y,di_z,di_m] = Simdata(G,x,y,z,d);

% input G is the background measured magnetic field gradient data
% inputs x, y and z are the respective coordinates of the field
% points input d is the bearing of the sensor in degrees from north
% output Sim_G is the simulated data, r and m are the true direction
% vectors and moment vectors for the simulated dipole, at location
% (di_x, di_y, di_z) with a magnetic moment di_m

n = size(G,1);

% Generate a location for the dipole and magnetic moment

rl = floor((0.3*rand+0.4)*n);
[di_x,di_y,di_z] = dipole_location(x(rl),y(rl));
    % location at ground level within 10 meters of input

di_m = dipole_mag_moment(1.5+rand(1));
    % random orientation vector with input magnitude

for j = 1:n
    h = (d(j)+90)*(2*pi)/360; angle of rotation from senor bearing
    r(j,:) = ([cos(h), -sin(h), 0;sin(h), cos(h),0;0, 0, 1]
                *[x(j)-di_x,y(j)-di_y,z(j)-di_z]’)’;
                % direction vector from dipole to field point
    m(j,:) = di_m;  %magnetic moment of the dipole
    di_G(j,:) = fwdeq(m(j,:),r(j,:)); %calculate field gradients
end

Sim_G = G + rotation(di_G);
    % rotates simulated dipole data from Euclidian bases
    % to sensor bases and adds it to the measured data
```

```
% make r unit vectors and adjust m accordingly

for i = 1:n
    rl = sqrt(r(i,:)*r(i,:)’);
    r(i,:) = r(i,:)/rl;
    m(i,:) = 3*m(i,:)/rlˆ4;
end
```

Signal to Noise

```
function [s,Ph]=snr(X,K,cyc,tol);

% input X is a matrix of N rows and P columns
% K is the dimension of the latent space
% output s is the SNR estimate for the P components of X

if nargin<4  tol=0.0001; end;
if nargin<3  cyc=100; end;

[N D]=size(X); D1=D;
tiny=exp(-700);

X=X-ones(N,1)*mean(X);
XX=X’*X/N;
diagXX=diag(XX);
ind=find(diagXX==0);

if length(ind)>0,
    X(:,ind)=[];
    XX=X’*X/N;
    diagXX=diag(XX);
    [N D1]=size(X);
    K=min(K,D1);
    ind=setdiff(1:D,ind);
end
if length(ind)==0, ind=1:D; end

L=pinv(real(sqrtm(XX)));
Ph=diag(XX);

I=eye(D);

lik=0; LL=[];

const=-D1/2*log(2*pi);

for i=1:cyc;

% E Step
  Phd=diag(1./Ph);
  LP=Phd*L;
  MM=Phd-LP*inv(I+L’*LP)*LP’;
  dM=max(sqrt(abs(det(MM))),tiny);
  beta=L’*MM;
  XXbeta=XX*beta’;
  EZZ=I-beta*L +beta*XXbeta;
```

```
% Compute log likelihood

  oldlik=lik;
  lik=N*const+N*log(dM)-0.5*N*sum(diag(MM*XX));
  LL=[LL lik];

% M Step

  L=XXbeta*inv(EZZ);
  Ph=diagXX-diag(L*XXbeta’);

  if (i<=2)
    likbase=lik;
  elseif (lik>=oldlik
            & ((lik-likbase)<(1+tol)*(oldlik-likbase)
                | ~finite(lik)))
    break;
  end;

end

s=zeros(D,1);

s(ind) = diagXX./Ph -ones(D1,1);
s(ind) = 10*log(s(ind))/log(10);
s = real(s);
```

Subspace Tracking Techniques

Singular Value Decomposition

```
function [r,m] = SST_SVD(G,win_size,num_pcs)

% input G is the magnetic field gradients
% input win_size is the temporal window length
% input num_pcs is the number of principal components
% used to recompose the filtered gradients
% output r is the estimated unit direction vector from the dipole
% output m is the estimated magnetic moment vector of the dipole

n = size(G,1);
midp = floor(win_size/2);
for i = 1:(n-win_size)
    [U,S,V] = svd(G(i:(win_size+i-1),:));
    Sh = zeros(size(S));
    Sh(4,4) = S(4,4);
    if num_pcs > 1
        Sh(5,5) = S(5,5);
        if num_pcs > 2
            Sh(6,6) = S(6,6);
        end
    end
    Gh = U*Sh*V’;

    dat= inverse_rotation(Gh);
        % removes the noisiest component and
        % rotates from the sensor bases to the Euclidian bases
```

```
    g=[dat(midp,1) dat(midp,2) dat(midp,3)
      dat(midp,2) dat(midp,4) dat(midp,5)
      dat(midp,3) dat(midp,5) -dat(midp,1)-dat(midp,4)];

    [r(i+midp+1,:),m(i+midp+1,:)] = frahm(g);
end
```

ULV Decomposition

```
function [r,m] = SST_ULV(G,win_size)

% input G is the magnetic field gradients
% input win_size is the temporal window length
% output r is the estimated unit direction vector from the dipole
% output m is the estimated magnetic moment vector of the dipole

% function hulv and ulv_win are part of the UTV toolbox
%
%  <References>
%    G.W. Stewart, "An Updating Algorithm for Subspace Tracking",
%    IEEE Trans. on SP, 40 (1992), pp. 1535--1541.
%
%  <Revision>
%    Ricardo D. Fierro, California State University San Marcos
%    Per Christian Hansen, IMM, Technical University of Denmark
%    Peter S.K. Hansen, IMM, Technical University of Denmark

n = size(G,1);
midp = floor(win_size/2);
[p,L,V,U,vec] = hulv(G(1:(win_size),:));

for i = 1:(n-win_size-1)
    Lh = L;
    sv = abs(sum(L,2));
    [ssv k] = sort(sv);
    Lh(k(1),:) = zeros(1,6);
    Lh(k(3),:) = zeros(1,6);
    Lh(k(4),:) = zeros(1,6);
    Lh(k(5),:) = zeros(1,6);

    Gh = U*L*V’;

    dat= inverse_rotation(Gh);
        % removes the noisiest component and
        % rotates from the sensor bases to the Euclidian bases

    g=[dat(midp,1) dat(midp,2) dat(midp,3)...
      dat(midp,2) dat(midp,4) dat(midp,5)...
      dat(midp,3) dat(midp,5) -dat(midp,1)-dat(midp,4)];

    [r(i+midp+1,:),m(i+midp+1,:)] = frahm(g);

    [p,L,V,U,vec] = ...
        ulv_win(p,L,V,U,G(i:(win_size+i-1),:),G(win_size+i,:));
end
```

Maximum Likelihood Estimation

```
function [r,m] = SST_MLE(Sim_G,win_size,sigma);

% input G is the magnetic field gradients
% input win_size is the temporal window length
% input sigma is the estimated std of the noise
% output r is the estimated unit direction vector from the dipole
% output m is the estimated magnetic moment vector of the dipole

dat = inverse_rotation(Sim_G);
       % removes the noisiest component and
       % rotates from the sensor bases to the Euclidian bases

g=[dat(:,1) dat(:,2) dat(:,3) dat(:,4) dat(:,5)];

opt = optimset(’fmincon’);
opt = optimset(opt,’Display’,’final’,’LargeScale’,’off’);

n = size(g,1);
midp = floor(win_size/2);
lb = [0,pi/2,0,pi/2,0,0];
ub = [2*pi,pi,2*pi,pi,2*pi,pi];

for i = 1:(n-win_size)
    R = (g(i:(win_size+i-1),:)’)*(g(i:(win_size+i-1),:))/win_size;
    theta0 = [pi,pi/4,pi,pi/4,2*pi*rand(1),pi*rand(1)];
    [theta er(i)] = fmincon(’mldoa’,theta0,[],[],[],[],lb,ub,[],opt,R,sigma);
    [D Nd md] = direct(theta);
    i
    r(i,:) = Nd;
    D_inv = pinv(D);
    m_temp = (D_inv*(g(i+midp,:)’))’;
    m(i,:) = m_temp(1,4)*md;
end

-----------------------------------------
function V = mldoa(Theta,R,sigma);

P_D = proj(Theta);

P_D_p = eye(size(P_D)) - P_D;

R_Inv = inv(R);

V = trace(P_D_p*(R+(sigmaˆ4)*R_Inv-2*(sigmaˆ2)*eye(size(R))));

-----------------------------------------
function P_D = proj(Theta);


Ne = [cos(Theta(1))*sin(Theta(2)), sin(Theta(1))*sin(Theta(2)), cos(Theta(2))];
Nd = [cos(Theta(3))*sin(Theta(4)), sin(Theta(3))*sin(Theta(4)), cos(Theta(4))];
m = [cos(Theta(5))*sin(Theta(6)), sin(Theta(5))*sin(Theta(6)), cos(Theta(6))];

D = [Nijk(Ne,1,1,1), Nijk(Ne,2,1,1), Nijk(Ne,3,1,1),
         m(1)*Nijk(Nd,1,1,1)+m(2)*Nijk(Nd,2,1,1)+m(3)*Nijk(Nd,3,1,1);...
     Nijk(Ne,1,1,2), Nijk(Ne,2,1,2), Nijk(Ne,3,1,2),
         m(1)*Nijk(Nd,1,1,2)+m(2)*Nijk(Nd,2,1,2)+m(3)*Nijk(Nd,3,1,2);...
```

```
     Nijk(Ne,1,1,3), Nijk(Ne,2,1,3), Nijk(Ne,3,1,3),
         m(1)*Nijk(Nd,1,1,3)+m(2)*Nijk(Nd,2,1,3)+m(3)*Nijk(Nd,3,1,3);...
     Nijk(Ne,1,2,2), Nijk(Ne,2,2,2), Nijk(Ne,3,2,2),
         m(1)*Nijk(Nd,1,2,2)+m(2)*Nijk(Nd,2,2,2)+m(3)*Nijk(Nd,3,2,2);...
     Nijk(Ne,1,2,3), Nijk(Ne,2,2,3), Nijk(Ne,3,2,3),
         m(1)*Nijk(Nd,1,2,3)+m(2)*Nijk(Nd,2,2,3)+m(3)*Nijk(Nd,3,2,3)];
P_D = D*inv(D’*D)*D’;

-----------------------------------------
function [D,Nd,m] = direct(Theta);

Ne = [cos(Theta(1))*sin(Theta(2)),
     sin(Theta(1))*sin(Theta(2)),
     cos(Theta(2))];

Nd = [cos(Theta(3))*sin(Theta(4)),
     sin(Theta(3))*sin(Theta(4)),
     cos(Theta(4))];

m = [cos(Theta(5))*sin(Theta(6)),
    sin(Theta(5))*sin(Theta(6)),
    cos(Theta(6))];

D = [Nijk(Ne,1,1,1), Nijk(Ne,2,1,1), Nijk(Ne,3,1,1),
         m(1)*Nijk(Nd,1,1,1)+m(2)*Nijk(Nd,2,1,1)+m(3)*Nijk(Nd,3,1,1);...
     Nijk(Ne,1,1,2), Nijk(Ne,2,1,2), Nijk(Ne,3,1,2),
         m(1)*Nijk(Nd,1,1,2)+m(2)*Nijk(Nd,2,1,2)+m(3)*Nijk(Nd,3,1,2);...
     Nijk(Ne,1,1,3), Nijk(Ne,2,1,3), Nijk(Ne,3,1,3),
         m(1)*Nijk(Nd,1,1,3)+m(2)*Nijk(Nd,2,1,3)+m(3)*Nijk(Nd,3,1,3);...
     Nijk(Ne,1,2,2), Nijk(Ne,2,2,2), Nijk(Ne,3,2,2),
         m(1)*Nijk(Nd,1,2,2)+m(2)*Nijk(Nd,2,2,2)+m(3)*Nijk(Nd,3,2,2);...
     Nijk(Ne,1,2,3), Nijk(Ne,2,2,3), Nijk(Ne,3,2,3),
         m(1)*Nijk(Nd,1,2,3)+m(2)*Nijk(Nd,2,2,3)+m(3)*Nijk(Nd,3,2,3)];
```

Bayesian Geometric Estimation

```
function [r,m] = SST_BAY(Sim_G,win_size,Po,sigma);

% input G is the magnetic field gradients
% input win_size is the temporal window length
% input Po is the prior knowledge of the projection
% input sigma is the estimated std of the noise
% output r is the estimated unit direction vector from the dipole
% output m is the estimated magnetic moment vector of the dipole

dat = inverse_rotation(Sim_G);
       % removes the noisiest component and
       % rotates from the sensor bases to the Euclidian bases

g=[dat(:,1) dat(:,2) dat(:,3) dat(:,4) dat(:,5)];

opt = optimset(’fmincon’);
opt = optimset(opt,’Display’,’final’,’LargeScale’,’off’);

n = size(g,1);
midp = floor(win_size/2);
lb = [0,pi/2,0,pi/2,0,0];
ub = [2*pi,pi,2*pi,pi,2*pi,pi];
```

```
for i = 1:(n-win_size)
    R = (g(i:(win_size+i-1),:)’)*(g(i:(win_size+i-1),:))/win_size;
    theta0 = [pi,pi/4,pi,pi/4,2*pi*rand(1),pi*rand(1)];
    [theta er(i)] = ...
        fmincon(’baydoa’,theta0,[],[],[],[],lb,ub,[],opt,R,Po,sigma,win_size);
    [D Nd md] = direct(theta);
    i
    r(i,:) = Nd;
    D_inv = pinv(D);
    m_temp = (D_inv*(g(i+midp,:)’))’;
    m(i,:) = m_temp(1,4)*md;
end

-----------------------------------------
function PUy = baydoa(Theta,R,Po,sigma,N);

P_D = proj(Theta);

[V, D] = eig(P_D);

Uo = V*sqrt(D);

Q = eye(5);;

del = 0.01;

Nu = ;

l=1;
U(:,:,1) = Uo;

for l = 1:700
    B = U(:,:,l)’QU(:,:,l)*K-K*U(:,:,l)’*Q*U(:,:,l);
    w = rand(25,1);
    SgwY = SgY(w);
    dU = -B*del + sqrt(2*del)*SgwY;
    U(:,:,l+1) = U(:,:,l)*exp(dU);
end;

A = squeeze(U(:,:,201))’*Q*squeeze(U(:,:,201));

for l = 202:700,
    A = A + squeeze(U(:,:,l))’*Q*squeeze(U(:,:,l));
end;

A = A/500;

Puy = (exp((N/sigma)*trace(P_D*R’))*exp(-norm(P_D-Po,2)/100))
        /(exp((N/sigma)*trace(A*R’))*exp(-norm(A-Po,2)/100));
```

References

[1] S. D. Billings, L. R. Pasion, and D. Oldenburg. UXO discrimination and identification using magnetometry. SAGEEP Conference, Las Vegas, Febuary 2002.

[2] S. D. Billings, L. R. Pasion, and D. Oldenburg. Discrimination and classification of UXO using magnetometry: Inversion and error analysis using robust statistics. SAGEEP Conference, San Antonio, April 2003.

[3] S.D. Billings. Discrimination and classification of buried unexploded ordnance using magnetometry. *IEEE Transactions on Geoscience and Remote Sensing*, 42(6):1241–1251, June 2004.

[4] D.K. Bulter, E.R. Cespedes, C.B. Cox, and P.J.Wolfe. Multisensor methods for buried unexploded ordnance detection, discrimination, and identification. Technical Report SERDP 98-10, U.S. Army Engineer Waterways Experiment Station, Vicksburg, MS, September 1998.

[5] J. Conway. *A Course in Functional Analysis*. Springer-Verlag, New York, 1990.

[6] C.M. Coviello, L.H. Sibul, and P.A. Yoon. Algebraic DOA estimation and tracking using ULV decomposition. In *Proceedings of the 2003 International Conference on Neural Networks and Signal Processing*, pages 1310–1313, 2003.

[7] K. Davis, Y. Li, and M.N. Nabighian. Automatic detection of UXO anomalies using extended Euler deconvolution. SAGEEP Atlanta, GA, April 2005.

[8] D. FitzGerald, A. Reid, and P. McInerney. New discrimination techniques for Euler deconvolution. *Computers and Geosciences*, 30:461–469, 2004.

[9] C.P. Frahm. Inversion of the magnetic field gradient equations for a magnetic dipole field. Technical Report NCSL 135-72, Naval Coastal Systems Laboratory, Panama City, Fla., Nov 1972.

[10] R.L.S. Hogg. Practicalities, pitfalls and new developments in airborne magnetic gradiometry. Technical report, Scott Hogg and Associates Ltd., PDAC presentation, March 2004.

[11] International campaign to ban landmines, http://www.icbl.org.

[12] A. G. Jaffer. Maximum likelihood direction finding of stochastic sources: A separable solution. In *ICASSP ’88*, pages 2893–2896, New York, 1988.

[13] M. C. Jeoffreys. Discrimination and identification of unexploded ordinances (UXO) using airborne magnetic gradients. In *Mathematics in industry study group*, pages 87–94, Johannesburg, 2004.

[14] X. Li and H.H. Fan. Blind channel identification: Subspace tracking method without rank estimation. *IEEE Transactions on Signal Processing*, 49(10):2372–2382, October 2001.

[15] J.S. Liu and R. Chen. Sequential Monte Carlo methods for dynamic systems. *Journal of the American Statistical Association*, 93:1032–1044, 1998.

[16] J.H. Lu and A. Weinstein. Poisson Lie groups, dressing transformations, and the bruhat decomposition. *Journal of Differential Geometry*, 31:501–526, 1990.

[17] F.T. Luk and S. Qiao. A new matrix decomposition for signal processing. *Automatica*, 30:39–43, Jan 1994.

[18] M. Moonen, P. van Dooren, and J. Vandewalle. A singular value decomposition updating algorithm for subspace tracking. *SIAM J. Matrix Anal. Appl.*, 13(4):1015–1038, 1992.

[19] E. Moulines, P. Duhamel, J. Cardoso, and S. Mayrargue. Subspace methods for the blind identification of multichannel fir filters. *IEEE Transactions on Signal Processing*, 43(2):516–525, Febuary 1995.

[20] M.N. Nabighian and R.O. Hansen. Unification of Euler and Werner deconvolution in three dimensions via the generalized Hilbert transform. *Geophysics*, 66:1805–1810, 2001.

[21] N. Pendock. Development of mathematical algorithms and software for the analysis of data derived from measurements of magnetic field gradients. Technical report, PicoImages, Johannesburg, December 2003.

[22] A. Srivastava. A bayesian approach to geometric subspace estimation. *IEEE Transactions on signal processing*, 48(5):1390–1400, May 2000.

[23] A. Srivastava and E. Klassen. Bayesian and geometric subspace tracking. *Advances in Applied Probability*, 36(1):43–56, March 2004.

[24] G. W. Stewart. An updating algorithm for subspace tracking. *IEEE Transactions on Signal Processing*, 40(6):1535–1541, June 1992.

[25] G. W. Stewart. On the early history of the singular value decomposition. *SIAM Rev.*, 35(4):551–566, 1993.

[26] A. Swindlehurst. Alternative algorithm for maximum likelihood DOA estimation and detection. *IEEE Proceedings F - Radar and Signal Processing*, December 1994.

[27] D.T. Thompson. EULDPH: a new techniques for making computer-assisted depth estimates from magnetic data. *Geophysics*, 47:31–37, 1982.

[28] United Nations. Assistance in mine clearance: Report of the Secretary-General, document A/49/357, September 1994.

[29] A. van der Veen, E. Deprettere, and A. Swindlehurst. Subspace-based signal analysis using singular value decomposition. *Proceedings of the IEEE*, 81(9):1277– 1308, September 1993.

[30] X. Wang and H.V. Poor. Blind equalization and multiuser detection in dispersive cdma channels. *IEEE Transactions on Communication*, 46(1):91–103, January 1998.